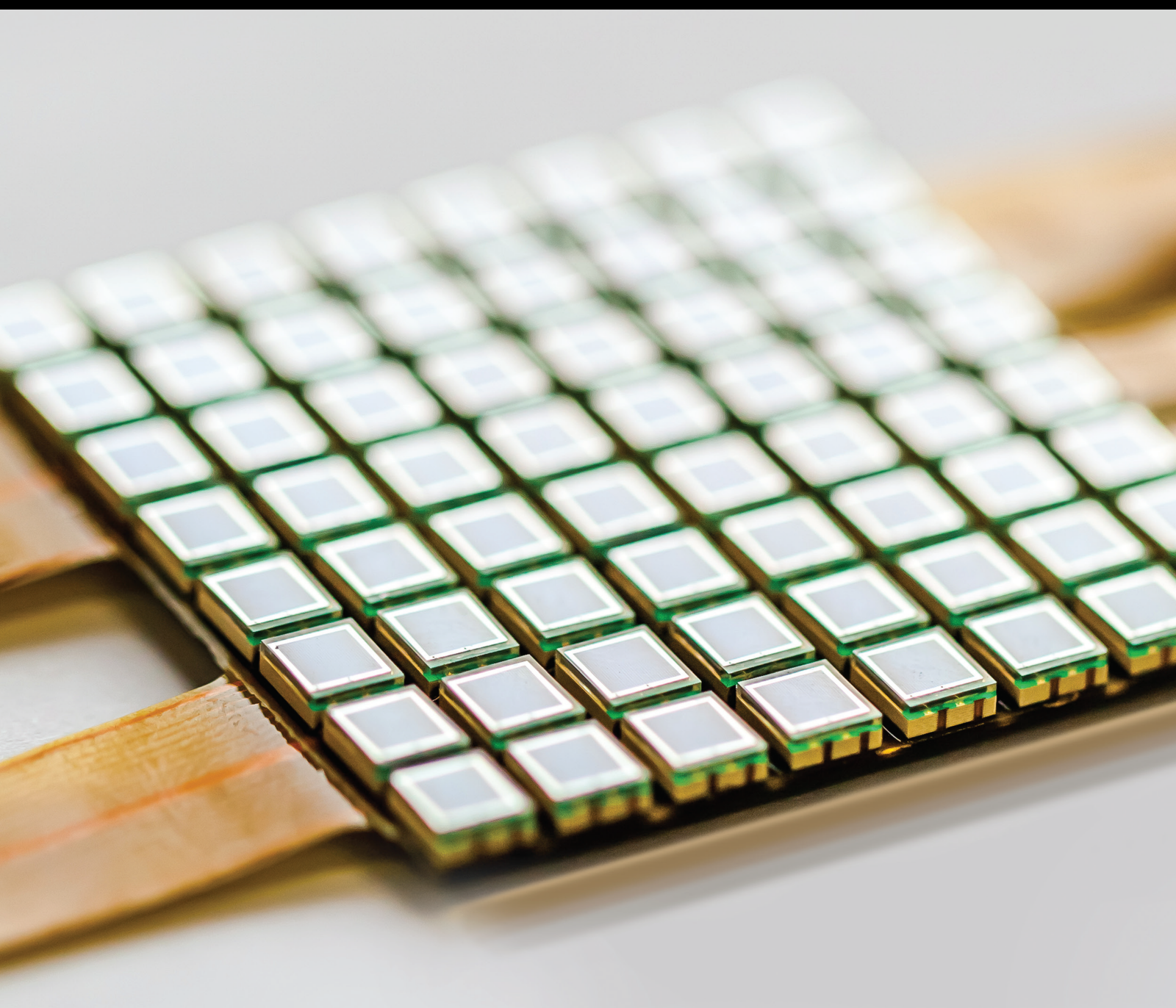


# Micro- and Nanotechnology for Sensing in Harsh Environments

Lead Guest Editor: Qiulin Tan

Guest Editors: Tao Luo and De-Zhi Wu





---

# **Micro- and Nanotechnology for Sensing in Harsh Environments**

Journal of Sensors

---

**Micro- and Nanotechnology for Sensing  
in Harsh Environments**

Lead Guest Editor: Qiulin Tan

Guest Editors: Tao Luo and De-Zhi Wu



---




Copyright © 2021 Hindawi Limited. All rights reserved.

This is a special issue published in "Journal of Sensors." All articles are open access articles distributed under the Creative Commons Attribution License, which permits unrestricted use, distribution, and reproduction in any medium, provided the original work is properly cited.

# Chief Editor

Harith Ahmad , Malaysia

## Associate Editors

Duo Lin , China  
Fanli Meng , China  
Pietro Siciliano , Italy  
Guiyun Tian, United Kingdom

## Academic Editors

Ghufran Ahmed , Pakistan  
Constantin Apetrei, Romania  
Shonak Bansal , India  
Fernando Benito-Lopez , Spain  
Romeo Bernini , Italy  
Shekhar Bhansali, USA  
Matthew Brodie, Australia  
Ravikumar CV, India  
Belén Calvo, Spain  
Stefania Campopiano , Italy  
Binghua Cao , China  
Domenico Caputo, Italy  
Sara Casciati, Italy  
Gabriele Cazzulani , Italy  
Chi Chiu Chan, Singapore  
Sushank Chaudhary , Thailand  
Edmon Chehura , United Kingdom  
Marvin H Cheng , USA  
Lei Chu , USA  
Mario Collotta , Italy  
Marco Consales , Italy  
Jesus Corres , Spain  
Andrea Cusano, Italy  
Egidio De Benedetto , Italy  
Luca De Stefano , Italy  
Manel Del Valle , Spain  
Franz L. Dickert, Austria  
Giovanni Diraco, Italy  
Maria de Fátima Domingues , Portugal  
Nicola Donato , Italy  
Sheng Du , China  
Amir Elzawwy, Egypt  
Mauro Epifani , Italy  
Congbin Fan , China  
Lihang Feng, China  
Vittorio Ferrari , Italy  
Luca Francioso, Italy

Libo Gao , China  
Carmine Granata , Italy  
Pramod Kumar Gupta , USA  
Mohammad Haider , USA  
Agustin Herrera-May , Mexico  
María del Carmen Horrillo, Spain  
Evangelos Hristoforou , Greece  
Grazia Iadarola , Italy  
Syed K. Islam , USA  
Stephen James , United Kingdom  
Sana Ullah Jan, United Kingdom  
Bruno C. Janegitz , Brazil  
Hai-Feng Ji , USA  
Shouyong Jiang, United Kingdom  
Roshan Prakash Joseph, USA  
Niravkumar Joshi, USA  
Rajesh Kaluri , India  
Sang Sub Kim , Republic of Korea  
Dr. Rajkishor Kumar, India  
Rahul Kumar , India  
Nageswara Lalam , USA  
Antonio Lazaro , Spain  
Chengkuo Lee , Singapore  
Chenzong Li , USA  
Zhi Lian , Australia  
Rosalba Liguori , Italy  
Sangsoon Lim , Republic of Korea  
Huan Liu , China  
Jin Liu , China  
Eduard Llobet , Spain  
Jaime Lloret , Spain  
Mohamed Louzazni, Morocco  
Jesús Lozano , Spain  
Oleg Lupan , Moldova  
Leandro Maio , Italy  
Pawel Malinowski , Poland  
Carlos Marques , Portugal  
Eugenio Martinelli , Italy  
Antonio Martinez-Olmos , Spain  
Giuseppe Maruccio , Italy  
Yasuko Y. Maruo, Japan  
Zahid Mehmood , Pakistan  
Carlos Michel , Mexico  
Stephen. J. Mihailov , Canada  
Bikash Nakarmi, China

Ehsan Namaziandost , Iran  
Heinz C. Neitzert , Italy  
Sing Kiong Nguang , New Zealand  
Calogero M. Oddo , Italy  
Tinghui Ouyang, Japan  
SANDEEP KUMAR PALANISWAMY ,  
India  
Alberto J. Palma , Spain  
Davide Palumbo , Italy  
Abinash Panda , India  
Roberto Paolesse , Italy  
Akhilesh Pathak , Thailand  
Giovanni Pau , Italy  
Giorgio Pennazza , Italy  
Michele Penza , Italy  
Sivakumar Poruran, India  
Stelios Potirakis , Greece  
Biswajeet Pradhan , Malaysia  
Giuseppe Quero , Italy  
Linesh Raja , India  
Maheswar Rajagopal , India  
Valerie Renaudin , France  
Armando Ricciardi , Italy  
Christos Riziotis , Greece  
Ruthber Rodriguez Serrezuela , Colombia  
Maria Luz Rodriguez-Mendez , Spain  
Jerome Rossignol , France  
Maheswaran S, India  
Ylias Sabri , Australia  
Sourabh Sahu , India  
José P. Santos , Spain  
Sina Sareh, United Kingdom  
Isabel Sayago , Spain  
Andreas Schütze , Germany  
Praveen K. Sekhar , USA  
Sandra Sendra, Spain  
Sandeep Sharma, India  
Sunil Kumar Singh Singh , India  
Yadvendra Singh , USA  
Afaque Manzoor Soomro , Pakistan  
Vincenzo Spagnolo, Italy  
Kathiravan Srinivasan , India  
Sachin K. Srivastava , India  
Stefano Stassi , Italy

Danfeng Sun, China  
Ashok Sundramoorthy, India  
Salvatore Surdo , Italy  
Roshan Thotagamuge , Sri Lanka  
Guiyun Tian , United Kingdom  
Sri Ramulu Torati , USA  
Abdellah Touhafi , Belgium  
Hoang Vinh Tran , Vietnam  
Aitor Urrutia , Spain  
Hana Vaisocherova - Lislalova , Czech  
Republic  
Everardo Vargas-Rodriguez , Mexico  
Xavier Vilanova , Spain  
Stanislav Vitek , Czech Republic  
Luca Vollero , Italy  
Tomasz Wandowski , Poland  
Bohui Wang, China  
Qihao Weng, USA  
Penghai Wu , China  
Qiang Wu, United Kingdom  
Yuedong Xie , China  
Chen Yang , China  
Jiachen Yang , China  
Nitesh Yelve , India  
Aijun Yin, China  
Chouki Zerrouki , France

## Contents

---

**Wireless Passive High-Temperature Sensor Readout System for Rotational-Speed Measurement**

Yingping Hong, Pengyu Jia, Xihao Guan, Jijun Xiong, Wenyi Liu, Huixin Zhang, and Chen Li 

Research Article (10 pages), Article ID 6656527, Volume 2021 (2021)

**Research on “Cylinder-Four-Beam” Microstructure Improvement of MEMS Bionic Vector**


**Hydrophone**

Zeming Jian , Yifan Huang , Lei Nie, Mengran Liu , and Guojun Zhang

Research Article (11 pages), Article ID 5580390, Volume 2021 (2021)

## Research Article

# Wireless Passive High-Temperature Sensor Readout System for Rotational-Speed Measurement

Yingping Hong,<sup>1,2</sup> Pengyu Jia,<sup>1,2</sup> Xihao Guan,<sup>1</sup> Jijun Xiong,<sup>1</sup> Wenyi Liu,<sup>1</sup> Huixin Zhang,<sup>1</sup> and Chen Li<sup>1,2</sup> 

<sup>1</sup>Science and Technology on Electronic Test and Measurement Laboratory, Taiyuan 030051, China

<sup>2</sup>Key Laboratory of Instrumentation Science and Dynamic Measurement, Ministry of Education, North University of China, Taiyuan 030051, China

Correspondence should be addressed to Chen Li; [lichen@nuc.edu.cn](mailto:lichen@nuc.edu.cn)

Received 22 December 2020; Revised 31 May 2021; Accepted 19 October 2021; Published 2 November 2021

Academic Editor: Alberto J. Palma

Copyright © 2021 Yingping Hong et al. This is an open access article distributed under the Creative Commons Attribution License, which permits unrestricted use, distribution, and reproduction in any medium, provided the original work is properly cited.

Rotational-speed measurement in harsh environments is an important topic. However, the high rotation results in rapid frequency variations in the signals of a sensor and changes in physical properties under extreme thermal circumstances cause significant difficulties in reading signals. To address this problem, we adopt wireless passive measurement methods to design a special characteristic signal circuit module that achieves precise measurement of rotational speed at high temperatures. The sensor and the readout system include a variable frequency source, a readout antenna, and a radio frequency demodulation circuit. Herein, a demodulation detector of the signal conversion circuit is designed and used in the envelope detection module of the single sideband demodulation method. In addition, a conversion circuit test platform for high-temperature environment sensor signal is developed. From the testing, the output signal demodulation of the sensor was observed under a maximum temperature of 700°C with error less than 0.12%. The new sensor and measurement method do not require physical leads and achieve wireless noncontact accurate measurement of rotational speed at high temperature.

## 1. Introduction

Rotational-speed sensors are widely used in aerospace, industrial control, traffic, and other fields, and the speed parameters in high-temperature environments are key for evaluating the working conditions of aero engines, space rocket engines, and ultra-high-speed turbo pumps [1–5]. However, the inability to obtain real-time and in situ information on the working state parameters such as the rotational speed of significant rotating components at high temperatures significantly affects the performance improvement of rotational speed devices in harsh environments. Consequently, there are several studies on related speed sensors.

Giebler et al. proposed a magnetic rotational sensors based on giant magnetoresistance (GMR) effect that were reliable at temperatures exceeding 170°C [6]. However, magnetic materials degauss at high temperatures; therefore,

GMR sensor is not suitable for high-temperature application. Huang et al. proposed that attaching two layers of hysteresis switches to count pulses, and angular speed can enable measurement with low uncertainties [7]. Li et al. designed a predetermined material stuck on the rotational shaft as an electrostatic sensor to measure rotational speed [8]. Tani et al. proposed a tribocharge sensor with a PTFE film. The film is charged by segmented electrodes, and the sensor can record approximately 2000 rpm [9]. Although the sensors have high dynamic response capability in high-speed measurement, in the low-speed area owing to the unstable electric charge, the time response is unsatisfactory, so it is not widely used. Lin and Ding proposed a method that measures the rotational speed of the engine from the lowest harmonic frequency component of its vibration signals [10]. Although this measurement method is simple and accurate, its high-temperature application is restricted.



Because noncontact detection of rotor rotating is feasible, imaging methods can be used to measure rotational speed. Kędzierski proposed a rotational-speed measurement calibration based on high-speed imaging [11]. The uncertainty of the method was calculated and tested with turbo-engines. Wang et al. [12] proposed that the rotational speed can be measured by a low-cost digital imaging device. Auto-correlation algorithms can calculate the rotational speed based the image without a marker on the rotor; although the measurement method has advantages such as noncontact measurement and high accuracy, its stability in harsh environments is limited. In addition, Gintner proposed a rotational-speed sensor with a soft magnetic core and a resonant circuit that operate up to 200°C and measures ranges of the sensor covers from static status to high speed [13]. Li et al. proposed sensors based on low temperature cofired ceramic (LTCC) [14]. Although the two sensors can operate in high-temperature environment, their dynamic response is unsatisfactory and cannot be used for precise measurement of rotational speed. For sensor readout system, vector network analyzers (VNAs) are widely used [15, 16]. In 2009, Nopper et al. presented a readout system for wireless passive sensors based on LC resonant circuits [17]. The system includes a coil as readout antenna, an LC resonator as sensor, an analog frontend, and a digital signal-processing unit. The analog frontend generates a frequency-variable signal to enable the digital signal-processing unit to detect the equivalent impedance of the readout coil. However, the sweep time limits high-speed sensing and the size of VNA, hindering its applicability. Moreover, wireless passives are also widely used in measurement. Several passive RFID sensors for temperature have been proposed. Wang et al. proposed temperature sense tag based on UHF RFID that can measure up to 120°C. UHF RFID is passive and has high sensitivity. Nonetheless, the current leaks across the PN-junctions with exponential growth at high temperatures and the chips cannot function [18]. The angle of the antenna pair affects the antenna gain and uncertainty [19].

To accurately measure the rotational speed in a high-temperature environment whereas ensuring a significant response speed and stability of the sensor, we propose a wireless passive sensor with square coils and parallel capacitors manufactured using thick film integration technology and corresponding data readout system. The readout system consists of a radio frequency (RF), signal generator, a readout antenna, and a directional coupler. Consequently, the fabricated rotational-speed sensor is suitable for high-temperature applications, and the readout system fulfils the requirement of responding to rapidly changing signals in high rotational speed sensing applications, such as rotational speed detection.

## 2. Sensor Principle

**2.1. Circuit Equipment Model.** As shown in Figure 1, the RF signal generating subsystem generates stimulus with variable frequency. For the rotor rotating, the lateral displacement between the sensor coil and the readout antenna changes periodically. Therefore, the rotational speed can be mea-

sured by detecting the coupling coefficient. The RF signal subsystem and directional coupler are 50Ω systems. The equipment impedance depends on input frequency and coupled coefficient. The impedance of readout antenna is

$$\underline{Z} = R_r + j\omega L_r + \frac{\omega^2 M^2}{R_s + j\omega L_s + (1/j\omega C_s)}, \quad (1)$$

where  $R_r$  is the series resistance of readout antenna,  $\omega = 2\pi f$  is the angular frequency, and  $M$  is the mutual inductance between the readout antenna and sensor inductor. For the 50Ω source, the reflection coefficient  $\Gamma$  is

$$\Gamma = \left. \left( \frac{\underline{Z} - Z_s}{\underline{Z} + Z_s} \right) \right|_{Z_s=50\Omega}. \quad (2)$$

If  $\underline{Z} > 50\Omega$ , the reflection coefficient  $\Gamma$  can be written as a

$$\Gamma = 1 - \frac{100}{\underline{Z} + 50}. \quad (3)$$

The directional coupler is a 3-port coupler and is connected reversely. The RF signal generator relates to transmitted port, and the readout antenna is connected to the input port. The reflection coefficient and  $Z$  are displayed in Figure 2.

Figure 2 shows the local minimum peak of reflection coefficient at a frequency slightly larger than the resonance frequency. The output of the directional coupler coupled terminal is

$$V_{cp} = C_{3,1}\Gamma = C_{3,1} \left( 1 - \frac{100}{50 + R_r + j\omega L_r + (\omega^2 M^2 / R_s + j\omega L_s (1/j\omega C_s))} \right), \quad (4)$$

where  $C_{3,1}$  is the coupling factor of directional coupler from the input port to the coupled port.

**2.2. Sensor Rotating Model.** The readout antenna measures coupling coefficient  $k$  to quantify the strength of the inductive coupling between the sensor and readout antenna. The coupling coefficient  $k$  describes the lateral displacement between the sensor and antenna. Using a high-temperature glue, the sensor was mounted on the motor. Therefore, the rotor and the lateral displacement between the sensor and antenna have a periodic variation of the same frequency in phase. The square coils are more useful and efficient compared to round coils [20]. Therefore, we use square coils with outmost turn  $l_0 = 40$  mm as readout antenna and sensor coils. Figure 3 shows a plot of the coupling coefficient  $k$  versus the lateral displacement between the sensor and the antenna.

From the simulation, the sensor  $S_{11}$  parameter is the smallest at 132 MHz, and  $S_{11} = -9.79$  dB. Therefore, in the speed parameter test, the frequency at the lowest value of  $S_{11}$  is selected as the excitation source frequency value. The

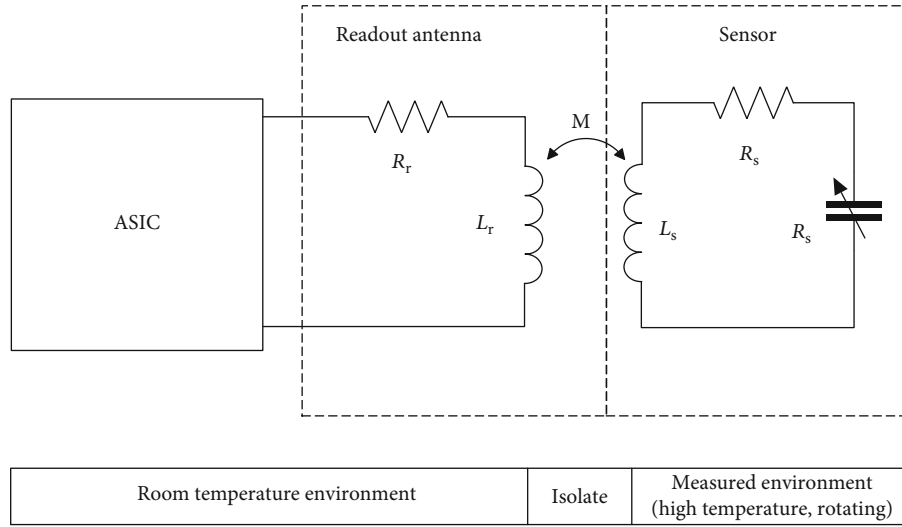


FIGURE 1: Schematic of the rotational-speed sensor system. The sensor circuit is inductively coupled to the readout antenna. The RF generator generates several frequency signal and detects the coupling coefficient.

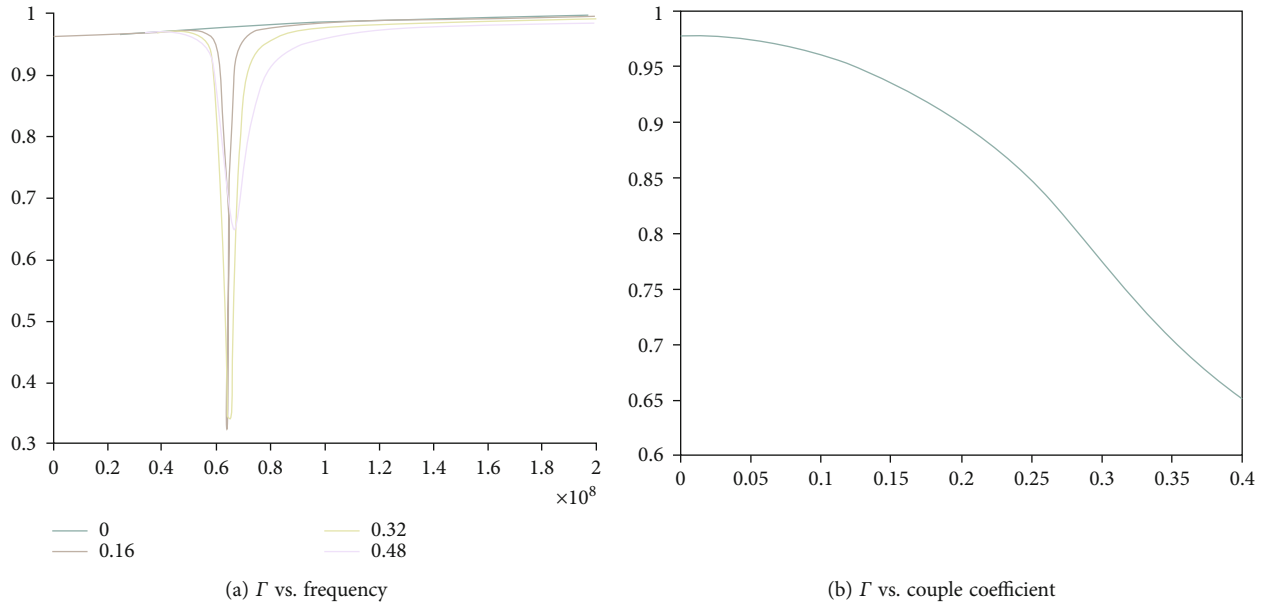


FIGURE 2: Simulated reflection coefficient  $\Gamma$  versus frequency and couple coefficient, for  $L_r = 100$  nH,  $R_r = 5\Omega$ ,  $k = 0.25$ ,  $f_0 = 100$  MHz, and  $Q = 8$ .

readout antenna  $S_{11}$  parameter can be written as

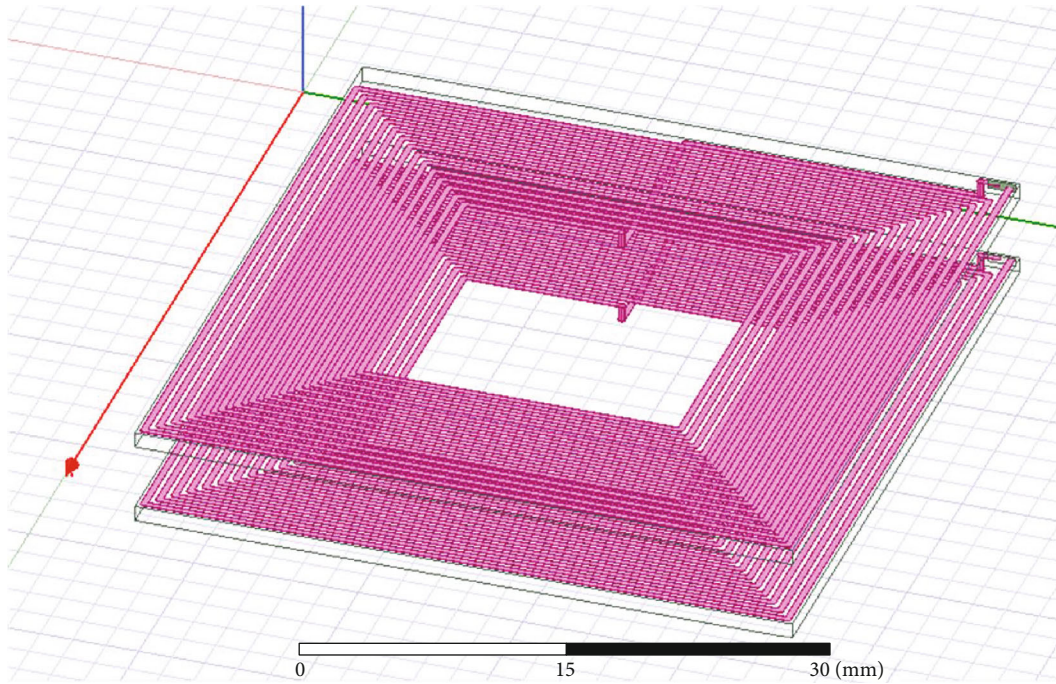
$$S_{11} = 20 \lg(\Gamma), \tag{5}$$

where  $\lg$  is the logarithm function and  $\Gamma$  is the reflection coefficient of the readout antenna. The measured output voltage can be converted to the  $S_{11}$  parameter that represents the coupling coefficient. Owing to the relative position of the antenna to the sensor derive couple coefficient, the reflect coefficient can be used to detect the relative position and rotational speed. Table 1 presents the simulated  $S_{11}$  parameter versus lateral displacement. From the data, we can derive the lateral displacement.

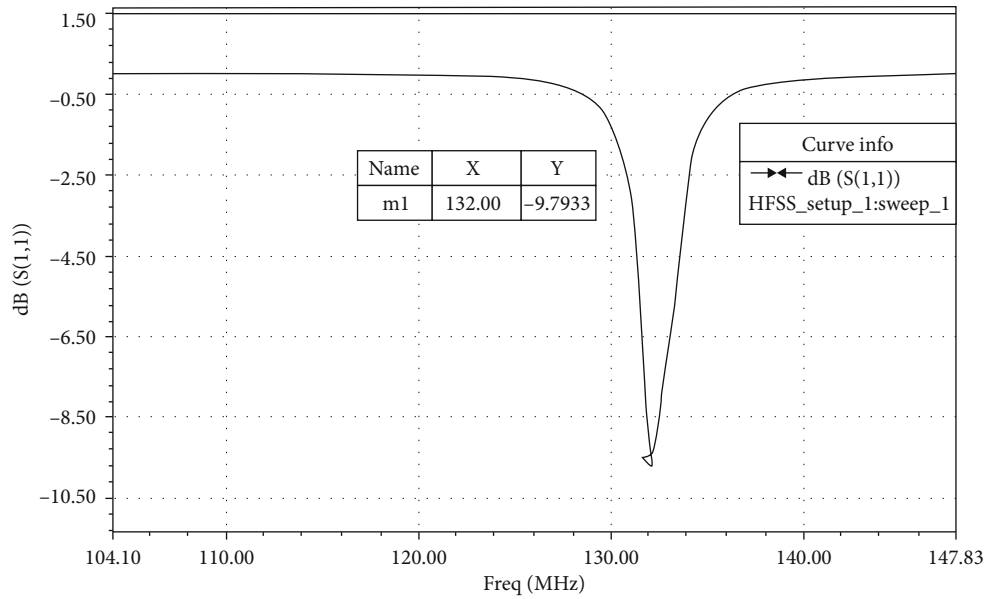
The periodic rotation of the rotor causes the sensor to approach and move away from the readout antenna periodically. In a small angle range, because the sensor approximately moves in a straight line, the lateral displacement is given by

$$d = r \sin \theta \approx \theta, \tag{6}$$

where  $d$  is the lateral displacement and  $r$  is the rotor radius. If the angle is larger than 19 mm, the sensor and the readout antenna are approximately uncoupled. In [19], Zierhofer and Hochmair investigated the lateral displacement against the coupling coefficient. We calculate  $V_{out}$  from Figure 4. The point where the lateral displacement is 0 mm between



(a) Simulated model for readout antenna and sensor



(b) Simulated S parameter of a single readout antenna

FIGURE 3: Simulated and calculated coupling coefficient versus lateral displacement between the sensor with the antenna. Both readout antenna and sensor outmost turn are  $l_0 = 40$  mm.

TABLE 1: Simulated  $S_{11}$  versus lateral displacement. The reflection coefficient is calculated by equipment.

| $L_d$ | $S_{11}$ (dB) | $L_d$ | $S_{11}$ (dB) | $L_d$ | $S_{11}$ (dB) | $L_d$ | $S_{11}$ (dB) |
|-------|---------------|-------|---------------|-------|---------------|-------|---------------|
| 0     | -13.59        | 5     | -8.84         | 10    | -5.80         | 15    | -3.30         |
| 1     | -12.18        | 6     | -8.04         | 11    | -5.50         | 16    | -2.04         |
| 2     | -10.57        | 7     | -7.91         | 12    | -4.30         | 17    | -1.22         |
| 3     | -9.73         | 8     | -7.86         | 13    | -3.54         | 18    | -0.74         |
| 4     | -9.52         | 9     | -6.66         | 14    | -3.52         | 19    | -0.47         |

In Table 1,  $L_d$  is the lateral displacement in millimeter.

the sensor and the antenna defines the 0 degrees. Figure 4 shows the algorithm that determines the rotational speed at a constant rotational speed. Whereas the rotor is rotating, the output  $V_{out}$  changes periodically with the same frequency.

In the rotation, if the LC resonator and the antenna are directly opposite, the impedance amplitude of the antenna end reaches the minimum value, and the voltage amplitude of the read antenna terminal reaches the minimum value. Therefore, in the rotation of the object, there will be a

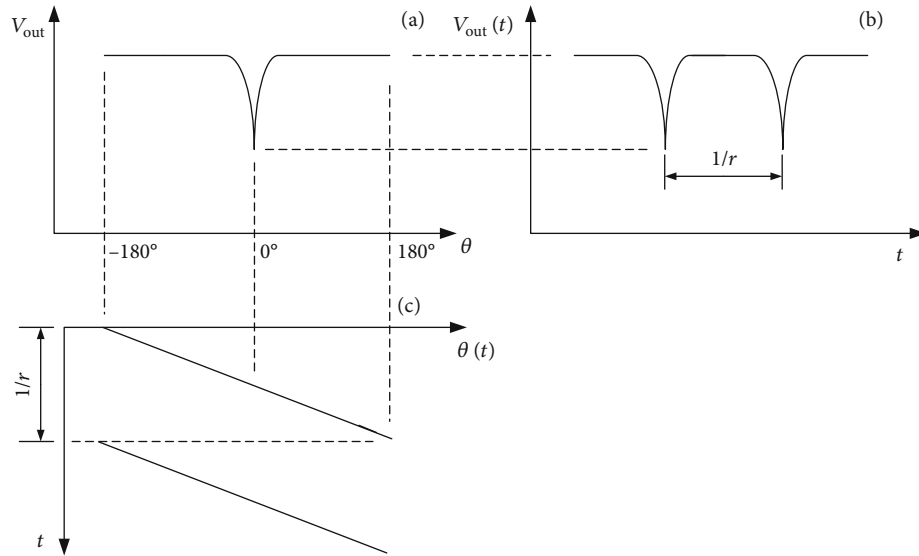


FIGURE 4: Principle of rotational speed detect algorithm (a) simulated  $V_{out}$  versus theta and (b) simulated  $V_{out}$  versus time, while the sensor is put on rotor with rotational speed of 60 r/min. (c) Theta versus time while the rotor is rotating.

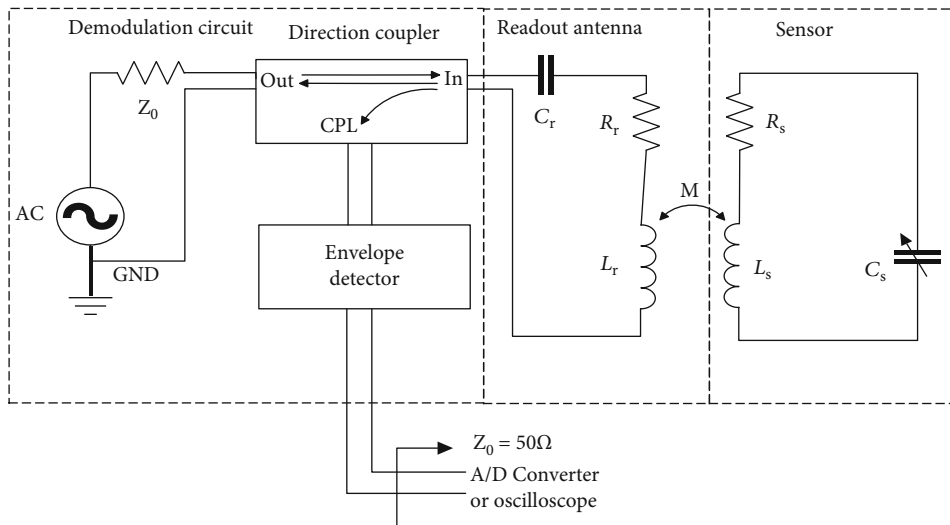


FIGURE 5: Lumped parameter circuit schematic view of the wireless rotational speed sensor system. RF signal generator generates a variable frequency signal. Directional coupler and ADC or oscilloscope collect RF reflected signal to determine the coupling coefficient. The sensor and the readout system convert the position information into a coil-coupling coefficient.

periodically changing voltage signal, and the amplitude decreases periodically, so that by tracking multiple trough points time interval to achieve the measurement of speed. Record the time of adjacent troughs as  $t_1$  and  $t_2$ , respectively,  $(t_1 - t_2)$  is the time interval between the LC resonator and the adjacent position of the reading antenna, and the rotation speed of the measured object is

$$v = \frac{1}{t_2 - t_1}. \quad (7)$$

2.3. *Single Tune Readout System.* Several studies have proposed detecting the sensor couple coefficient using the real part of the impedance with sweep frequency [13–15]. However, the sensor couple coefficient can be detected using a

single point reflect coefficient. This method prevents the generation of scan frequency signals. Therefore, the overall system has a higher response time, and no sweep generator reduces the system’s size and cost. Figure 5 shows the proposed structure. It has a PLL that generates an RF voltage signal,  $V_s = |V_s| \sin 2\pi ft$ . A Texas instruments PLL atinum RF synthesizer LMX2571, with a delta-sigma fractional  $N$ . The PLL is used to generate the voltage signal. The output frequency of LMX2571 can be set through a microwire digital interface. This RF voltage signal drives the readout antenna. Whereas the impedance of the antenna device changes with the coupling condition, the reflected echo changes. Thus, the echo signal can be extracted with the directional coupler ZEDC-10-2B from Mini-Circuits. The ZEDC10-2B is a wideband, 1 to 1000 MHz, and 3-port

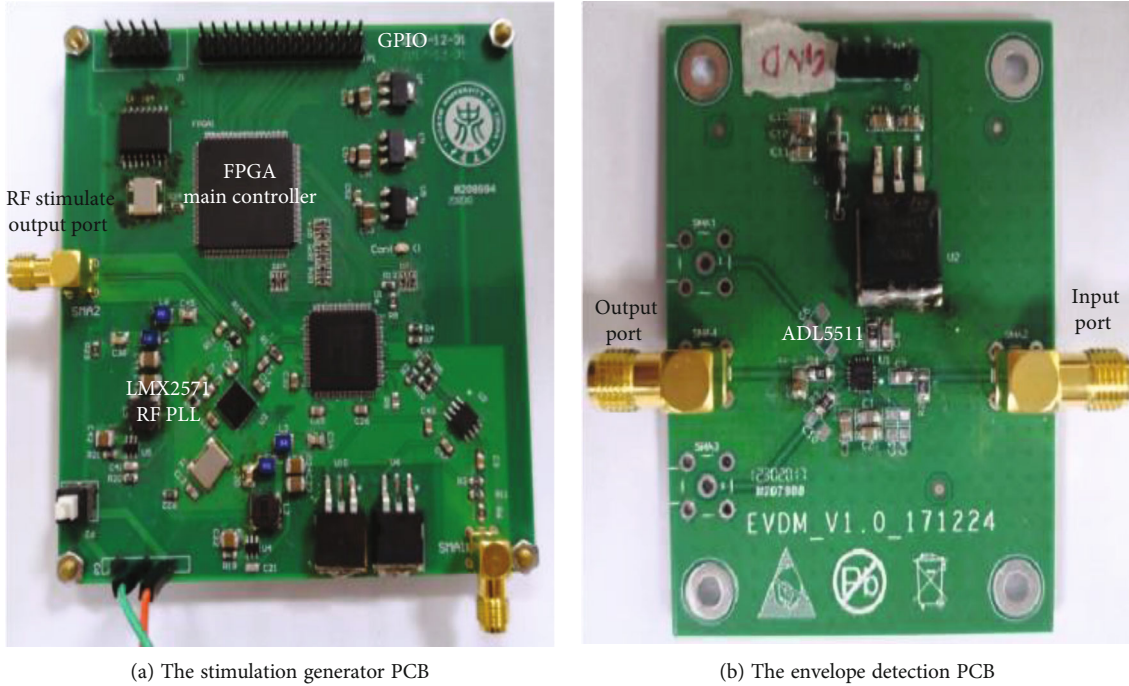


FIGURE 6: Prototype of the sensor demodulating circuit. The prototype includes two PCBs: the (a) one is RF stimulation PCB, and it provides an adjustable stimulation; the (b) one is envelope detection PCB, and it is used to demodulate the reflect signal of antenna and sensor. The stimulate frequency can be adjusted by the GPIO interface, and the output stimulate voltage  $V_{out}$  is fed to the left subminiature version B (SMB) connector.

TABLE 2: Sensor’s geometrical structure parameter.

| Parameter  | Symbol | Value   |
|--|--------|---------|
| Edge length of the outermost turn of the sensor coil | $d_o$  | 40.0 mm |
| Edge length of the innermost turn of the sensor coil | $d_i$  | 11.6 mm |
| Edge length of parallel plate capacitor              | $d_c$  | 6 mm    |
| Number of coils                                      | $N$    | 15      |
| The thickness of the ceramic substrate               | $w$    | 0.35 mm |
| Width of conductor                                   | $l_w$  | 0.4 mm  |

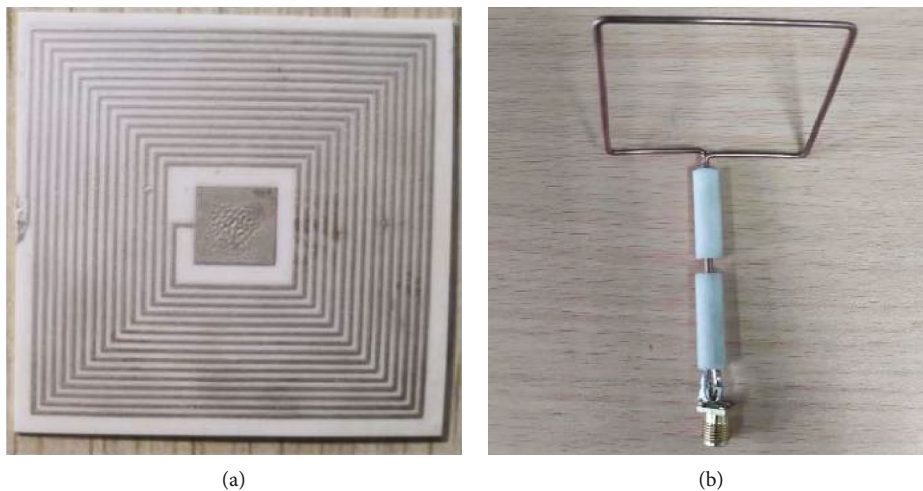


FIGURE 7: Sensor based on 95% alumina substrate. The pattern of readout antenna is consistent with the sensor and based on FR-4 substrate: (a) the figure of fabricated sensor; (b) figure of fabricated readout antenna.

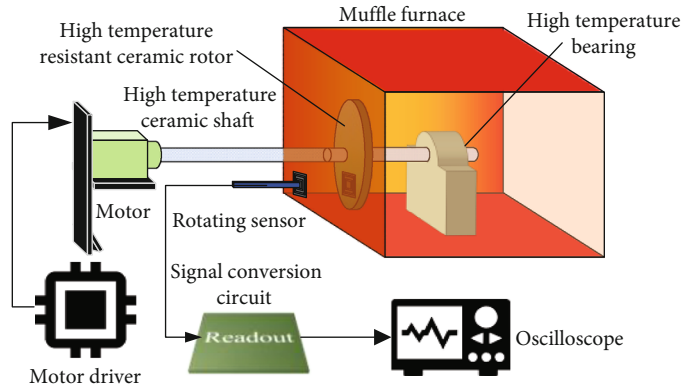


FIGURE 8: System architecture of the test bench. A high-temperature tolerance bearing is used to hold the rotating shaft made with alumina ceramic.

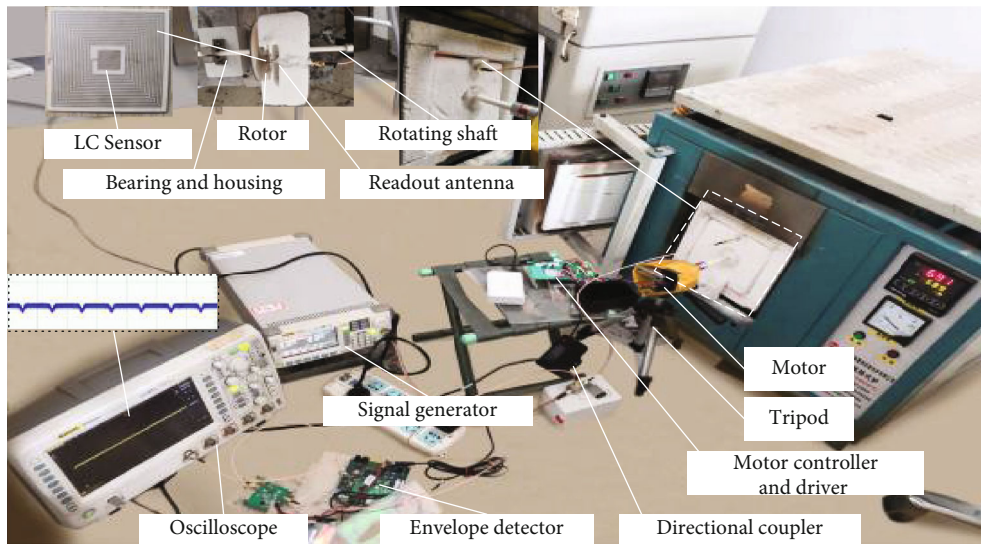


FIGURE 9: The prototype of the test bench. The high-temperature environment is dominated by a BLMT-1800.

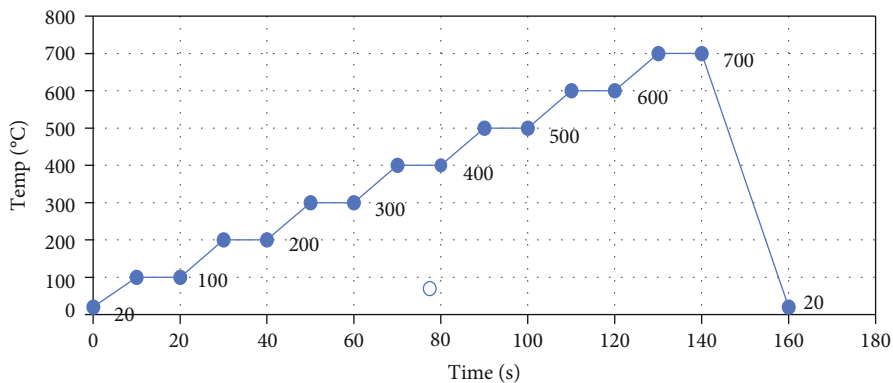


FIGURE 10: The temperature-time curve of the sensor testing.

directional coupler. The directional coupler couples the reflected echo to the coupled port. Consequently, the output of the coupled port of directional coupler is proportional to the reflection coefficient. An analog device envelope detector detects the envelope of the coupled port, and the envelope output is proportional to amplitude. The system output is

$$V_{out} = G_{env} V_{cp}, \tag{8}$$

where  $V_{out}$  is the system output and  $G_{env}$  is the conversion gain of envelope detector. In ADL5511, the normal conversion gain is 1.46 V/V. Subsequently, the envelope output

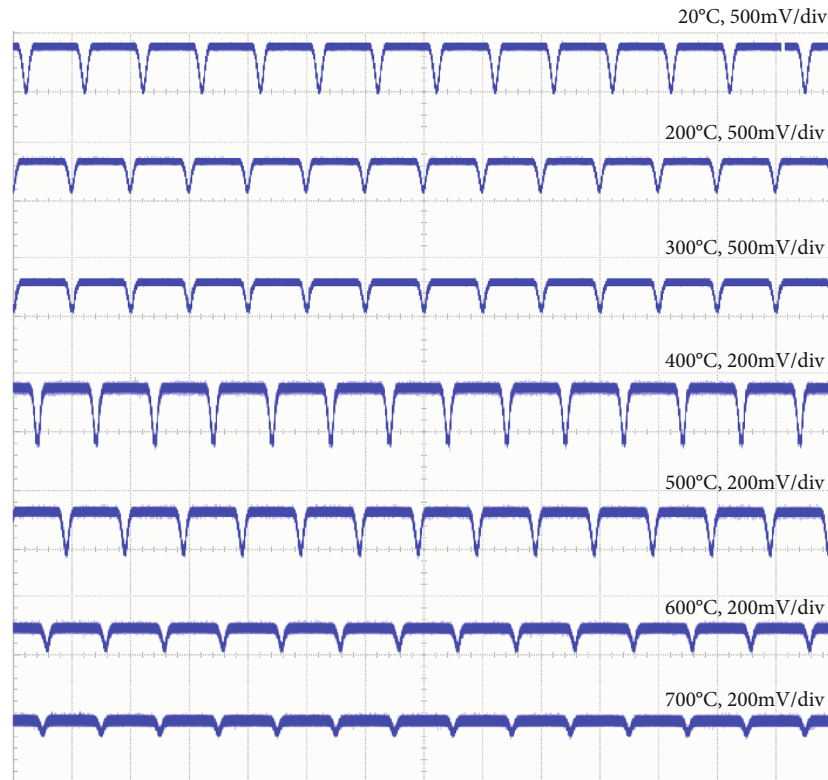


FIGURE 11: Sensor and signal conversion circuit test results. The test temperature rises one by one, from 20°C to 700°C; all curve horizontal scale is 1 s/div.

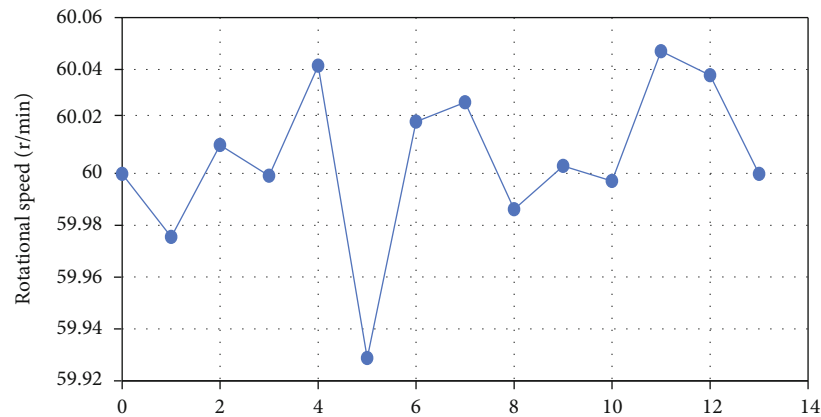


FIGURE 12: The calculated rotational speed of the sensor testing.

can be measured by analog-digital converter (ADC) or oscilloscope.

A prototype of the proposed frontend circuit is built using commercially available analog integrated circuits (ICs) on a printed circuit board. The prototype is depicted in Figure 6.

**2.4. Sensor Geometrical and Fabrication.** From [19], the working frequency of the sensor is closely related to the geometric size of the sensor. From the simulation, the number of coil turns has significant impact on the coil's own inductance and the sensor's quality factor. From the computations and comparisons, we determined the following structural parameters. The reasonable size of the sensor is presented in Table 2.

In standard thick film integration technology, the sensor is sintered using a 95% alumina substrate and silver paste. The top of the 1st layer and the bottom of the 3rd layer were screen printed on the silver pattern in the initial step. All layers of tape were stacked and laminated. Thereafter, the stack was placed into a box furnace and applied a high temperature to shape the sensor. An image of the fabricated sensor is shown in Figure 7.

### 3. Experiment and Discussion

To investigate the readout system, a rotational speed test bench was developed. Figures 8 and 9 present the full view

of the test bench. The sensor is glued to the turn plate that is held using a bearing. Thereafter, the plate is placed into the muffle furnace, and the motor is used to rotate the sensor at a constant speed.

The readout antenna is coupled with the rotating sensor at 5 mm distance. The antenna is connected to the readout system whereas the output of the readout system is connected to a rigol DS6064 oscilloscope.

Initially, the sensor resonance frequency is determined at room environment from the ANSYS electronic simulation result. Thereafter, the temperature rise curve of the muffle furnace is set based on the temperature curve from Figure 10. Each set temperature point is maintained for 10 min to measure the sensor working output. A driver is set to drive a stepper motor to rotate at a speed of 60 r/min in the entire process. We measured the output from room temperature to 700°C; the outputs are indicated in Figure 11. If the temperature ranges from 20°C to 500°C, the scales of output curve are 500 mV/div. At temperatures above 500°C, the scales of output curve are 200 mV/div. As the temperature rises, the peak of output reduces, owing to the rapid increase of the quality factor  $Q$ . The results are shown in Figure 12.

#### 4. Conclusion

This study proposes a sensor readout system for rotational-speed measurement and uses a novel method to achieve the measurement of rotational speed at high temperatures. By introducing a sine excitation to the readout antenna, the amplitude of its reflected signal was measured to obtain the equivalent impedance. To address the weakening of signal under high temperature, we designed an amplifying circuit to address the sensitive detection problem. In addition, we developed a rotational speed-temperature composite test platform and tested the sensor using the muffle furnace. From the test, the given rotational speed signal can be measured under 700°C with an error of less than 0.12%. This depicts the effectiveness of the sensor in high-temperature environments.

#### Data Availability

The data used to support the findings of this study are included within the article.

#### Conflicts of Interest

There is no conflict of interest regarding the publication of this paper.

#### Acknowledgments

This work is supported by the China Postdoctoral Science Foundation (No. 2019M661071), the China Aviation Development Group Industry-University-Research Cooperation Project (No. HFZL2020CXY019), and the National Natural Science Foundation of China Youth Fund Project (No. 51705475 and No. 51705478).

#### References

- [1] C. Pan, L. Chen, L. Chen, H. Jiang, Z. Li, and S. Wang, "Research on motor rotational speed measurement in regenerative braking system of electric vehicle," *Mechanical Systems and Signal Processing*, vol. 66-67, pp. 829–839, 2016.
- [2] L. Wang, Y. Yan, and K. Reda, "Comparison of single and double electrostatic sensors for rotational speed measurement," *Sensors and Actuators A: Physical*, vol. 266, pp. 46–55, 2017.
- [3] C. Chen, T. Ma, H. Jin, Y. Wu, Z. Hou, and F. Li, "Torque and rotational speed sensor based on resistance and capacitive grating for rotational shaft of mechanical systems," *Mechanical Systems and Signal Processing*, vol. 142, article 106737, 2020.
- [4] Z. Xie, J. Dong, Y. Li et al., "Trielectrostatic rotational speed sensor integrated into a bearing: a solid step to industrial application," *Extreme Mechanics Letters*, vol. 34, article 100595, 2020.
- [5] L. Wang, Y. Yan, Y. Hu, and X. Qian, "Rotational speed measurement through electrostatic sensing and correlation signal processing," *IEEE Transactions on Instrumentation and Measurement*, vol. 63, no. 5, pp. 1190–1199, 2014.
- [6] C. Giebler, D. Adelerhof, A. Kuiper, J. B. A. van Zon, D. Oelgeschläger, and G. Schulz, "Robust GMR sensors for angle detection and rotation speed sensing," *Sensors and Actuators A: Physical*, vol. 91, no. 1-2, pp. 16–20, 2001.
- [7] H. Huang, W. Chou, and Z. Zhang, "A high-performance angular speed measurement method based on adaptive hysteresis switching techniques," *Mechanical Systems and Signal Processing*, vol. 64-65, pp. 282–295, 2015.
- [8] L. Li, H. Hu, Y. Qin, and K. Tang, "Digital approach to rotational speed measurement using an electrostatic sensor," *Sensors*, vol. 19, no. 11, p. 2540, 2019.
- [9] H. Tani, D. OKISHIO, R. Lu, S. Koganezawa, and N. Tagawa, "Development of tribocharge rotational speed sensor for rolling bearing," in *The Proceedings of the Conference on Information, Intelligence and Precision Equipment: IIP*, vol. 2018, Japan, 2018.
- [10] H. Lin and K. Ding, "A new method for measuring engine rotational speed based on the vibration and discrete spectrum correction technique," *Measurement*, vol. 46, no. 7, pp. 2056–2064, 2013.
- [11] Ł. Kędzierski, "High speed imaging method for rotational speed calibration," *Przegląd Elektrotechniczny*, vol. 1, no. 5, pp. 186–189, 2019.
- [12] T. Wang, Y. Yan, L. Wang, Y. Hu, and S. Zhang, "Instantaneous rotational speed measurement using image correlation and periodicity determination algorithms," *IEEE Transactions on Instrumentation and Measurement*, vol. 69, no. 6, pp. 2924–2931, 2020.
- [13] K. Gintner, "Rotational Speed Sensor for High Temperature," in *18. Internationales Stuttgarter Symposium*, M. Bargende, H.-C. Reuss, and J. Wiedemann, Eds., pp. 761–772, Springer Fachmedien Wiesbaden, Wiesbaden, 2018.
- [14] C. Li, Q. Tan, P. Jia et al., "Review of research status and development trends of wireless passive LC resonant sensors for harsh environments," *Sensors*, vol. 15, no. 6, pp. 13097–13109, 2015.
- [15] M. Sun, Y.-Q. Zhang, Y.-X. Guo, M. F. Karim, O. L. Chuen, and M. S. Leong, "Integration of circular polarized array and Ina in LTCC as a 60-GHz active receiving antenna," *IEEE Transactions on Antennas and Propagation*, vol. 59, no. 8, pp. 3083–3089, 2011.



- [16] C. Li, Q. Tan, C. Xue, W. Zhang, Y. Li, and J. Xiong, "A high-performance LC wireless passive pressure sensor fabricated using low-temperature co-fired ceramic (LTCC) technology," *Sensors*, vol. 14, no. 12, pp. 23337–23347, 2014.
- [17] R. Nopper, R. Has, and L. Reindl, "A wireless sensor readout system—circuit concept, simulation, and accuracy," *IEEE Transactions on Instrumentation and Measurement*, vol. 60, no. 8, pp. 2976–2983, 2011.
- [18] B. Wang, M.-K. Law, J. Yi, C.-Y. Tsui, and A. Bermak, "A -12.3 DBm UHF passive RFID sense tag for grid thermal monitoring," *IEEE Transactions on Industrial Electronics*, vol. 66, no. 11, pp. 8811–8820, 2019.
- [19] J. Hannula and V. Viikari, "Uncertainty analysis of intermodulation based antenna measurements," in *2016 10th European Conference on Antennas and Propagation (EuCAP)*, pp. 1–5, Davos, Switzerland, 2016.
- [20] C. M. Zierhofer and E. S. Hochmair, "Geometric approach for coupling enhancement of magnetically coupled coils," *IEEE Transactions on Biomedical Engineering*, vol. 43, no. 7, pp. 708–714, 1996.

## Research Article

# Research on “Cylinder-Four-Beam” Microstructure Improvement of MEMS Bionic Vector Hydrophone

Zeming Jian <sup>1</sup>, Yifan Huang <sup>1</sup>, Lei Nie<sup>1</sup>, Mengran Liu <sup>1</sup> and Guojun Zhang<sup>2</sup>

<sup>1</sup>Hubei Key Laboratory of Modern Manufacturing Quantity Engineering, School of Mechanical Engineering, Hubei University of Technology, Wuhan, Hubei 430068, China

<sup>2</sup>Key Laboratory of Instrumentation Science & Dynamic Measurement, Ministry of Education, North University of China, Taiyuan 030051, China

Correspondence should be addressed to Mengran Liu; [liumengran1991@163.com](mailto:liumengran1991@163.com)

Received 8 January 2021; Accepted 11 May 2021; Published 9 June 2021

Academic Editor: De-Zhi Wu

Copyright © 2021 Zeming Jian et al. This is an open access article distributed under the Creative Commons Attribution License, which permits unrestricted use, distribution, and reproduction in any medium, provided the original work is properly cited.

The existing MEMS bionic vector hydrophone has the problems of low-sensitivity and narrow-working band, and the sensitivity and working bandwidth cannot be improved simultaneously by changing the single microstructural parameter. In this paper, the MEMS bionic vector hydrophone microstructural parameters (length, width and height of cantilever, side length of the center block, height and radius of the rigid cylinder) have been optimized simultaneously to obtain a higher sensitivity at the almost same working bandwidth. Firstly, through the mechanical analysis of the microstructure, the objective function and feasible region are established to optimize the parameters of the microstructure, and a set of optimized parameters is obtained. Secondly, the optimized structure is verified by ANSYS simulation, and then, the optimized four-beam structure is fabricated by the MEMS manufacturing technology. Finally, these two kinds of hydrophones (the previous one and the optimized one) are produced, and their performance tests are carried out. The testing results show that the performances of the optimized hydrophone have been greatly improved, exhibiting a receiving sensitivity of  $-181.2$  dB@1 kHz (increasing by 6.5 dB, 0 dB reference  $1$  V/ $\mu$ Pa), the frequency response ranging from 20 Hz to 1 kHz which is the same working bandwidth as before, and a good dipole directivity. The optimization researches in this paper provide a method and idea for the performance improvement of the following MEMS vector hydrophone.

## 1. Introduction

With the continuous consumption of land resources, the huge resources in the deep ocean will become precious and provide the abundant substances that human beings need to live by including the energy, mine, and biology [1, 2]. Sonar system is the key equipment to obtain information from the ocean. And vector hydrophone as an important part of the sonar detection devices can measure vibrating acceleration of water particle and has the advantage of noise cancellation due to its directional pattern [3–6]. Faced with the increasingly serious underwater security situation, it urgently needs to adopt new technologies and methods to meet the requirements of engineering application. MEMS technology, due to the characteristic of 3M (miniaturization, multiplicity

and microelectronics), shows great vitality [7–10]. To this end, scholars expect to resolve current problems of large volume, poor consistency, and high cost through MEMS technology.

MEMS bionic vector hydrophone based on the bionic principle, piezoresistive principle, and MEMS technology, invented by the North University of China in 2007, is shown in Figure 1 [11], which has advantages of small volume, good consistency, and wonderful low frequency effect [11, 12].

However, the hydrophone has the problems of low sensitivity and narrow working bandwidth [13, 14]. In recent years, a lot of efforts have been put into the MEMS vector hydrophone to improve its sensitivity. The “Lollipop-shaped” structure MEMS vector hydrophone was produced by Liu et.al [15], and a stress centralized structure MEMS

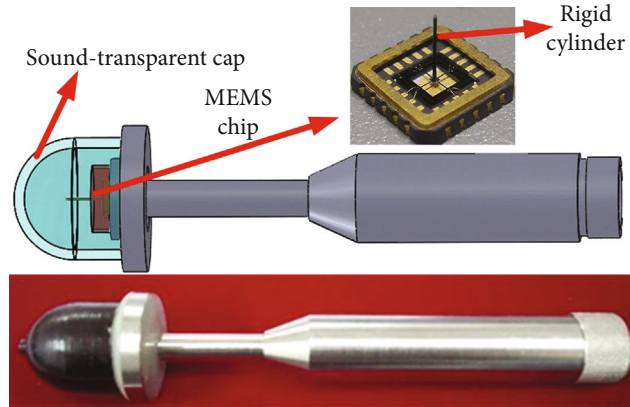
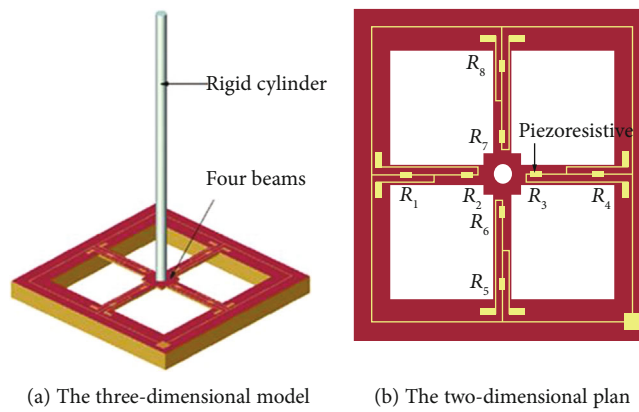


FIGURE 1: MEMS bionic vector hydrophone.



(a) The three-dimensional model (b) The two-dimensional plan

FIGURE 2: The view of the hydrophone microstructure.

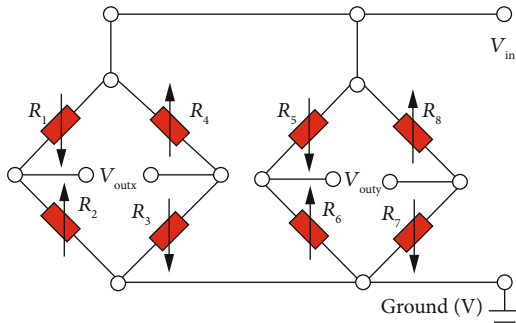


FIGURE 3: Diagram of Wheatstone bridge.

vector hydrophone was presented by Zhang et al. [16]. Although these two structures, respectively, improved the sensitivity of the hydrophones, it greatly reduced their working bandwidth. The sensitivity of the hydrophone has been also improved by replacing the previous cylinder structure with five different new structures, which are, respectively, the cup-shaped MEMS vector hydrophone designed by Xu et al. [17], the two-component cilia cylinder MEMS vector hydrophone proposed by Xu et al. [18], the cilia cluster MEMS vector hydrophone developed by Zhang et al. [19], the dumbbell-shaped ciliary MEMS vector hydrophone reported by Ji et al. [20], and the hollow cilium cylinder vec-

tor hydrophone presented by Yang et al. [21]. However, they increased varying degrees of the difficulty of the hydrophone fabricating process and reduced the consistency of the hydrophone production. And, in reference [21], they did not take into account that the hollow cilium cylinder structure is prone to bubble forming, which has destructive effects on the performance of the hydrophone.

Furthermore, all of the above studies only improved the sensitivity of MEMS hydrophones by changing the cylinder structure or four-beam microstructure alone, without optimizing and improving both. In this paper, through theoretical analysis and derivation, the maximum stress on the beam and the natural frequency of the microstructure are opposite trend changing with each parameter (length, width and height of cantilever, side length of the center block, height and radius of the rigid cylinder) of the microstructure. However, the influence weight of each parameter on the maximum stress and the natural frequency is different. Therefore, the parameters of cylinder structure and four-beam microstructure are optimized simultaneously, aiming to further improve the sensitivity of the hydrophone and retain the same working bandwidth.

## 2. Working Principles

MEMS bionic vector hydrophone microstructure includes four beams, a rigid cylinder fixed in the middle of the four

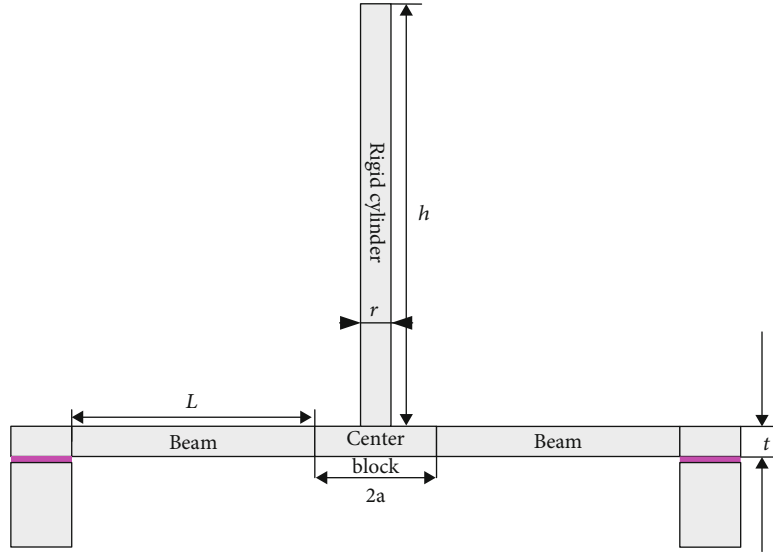


FIGURE 4: The cross-sectional view of the MEMS bionic vector hydrophone microstructure.

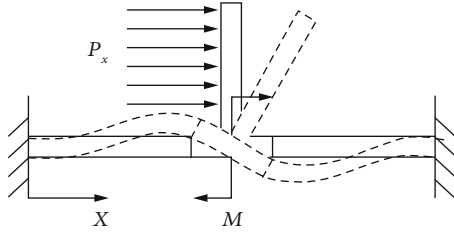


FIGURE 5: Microstructural deformation.

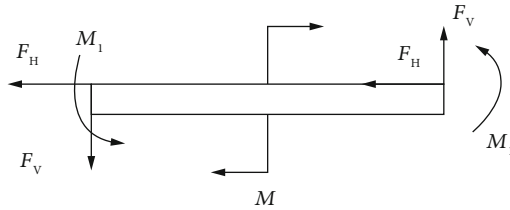


FIGURE 6: The force analysis diagram of the center block.

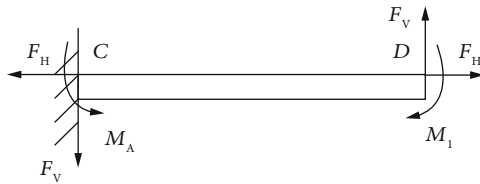


FIGURE 7: Force analysis diagram of a single cantilever beam.

beams, and eight equal strain pizeoresistors in the edge of four beams (as shown in Figure 2) [22]. Figure 2(a) is the three-dimensional model; Figure 2(b) is the two-dimensional plan. Eight equal strain pizeoresistors constitute two Wheatstone bridges (as shown in Figure 3).

When sound waves cause vibration of rigid cylinder and make four beams deformed, the stress on four beams will cause the resistance change of the pizeoresistors. Thus, we

can get the sound information from the outputs ( $V_{\text{outx}}$  and  $V_{\text{outy}}$ ) of the Wheatstone bridge.

The output voltage of the first Wheatstone bridges can be expressed as

$$V_{\text{outx}} = \frac{(R_1 + \Delta R_1)(R_3 + \Delta R_3) - (R_2 - \Delta R_2)(R_4 - \Delta R_4)}{(R_1 + \Delta R_1 + R_2 - \Delta R_2)(R_3 + \Delta R_3 + R_4 - \Delta R_4)} V_{\text{in}}. \quad (1)$$

When  $R_1 = R_2 = R_3 = R_4$  and  $\Delta R_1 = \Delta R_2 = \Delta R_3 = \Delta R_4 = \Delta R$ ,

$$V_{\text{outx}} = \frac{\Delta R}{R} V_{\text{in}}. \quad (2)$$

For the P-type strain pizeoresistors [22, 23],

$$\frac{\Delta R}{R} \approx 71.8 \sigma_l \times 10^{-11}. \quad (3)$$

Therefore, formula (3) can be approximated by:

$$V_{\text{outx}} = 71.8 \times 10^{-11} \times \sigma_l \times V_{\text{in}}, \quad (4)$$

where  $\sigma_l$  is component of longitudinal stress;  $V_{\text{in}}$  is the input voltage, and  $V_{\text{in}} = 10 \text{ V}$ . From formula (4), we can conclude that the output ( $V_{\text{outx}}$ ) of the Wheatstone bridge is proportional to the stress on the beam.

### 3. Optimization Design

**3.1. Microstructure Analysis.** The cross-sectional view of the MEMS bionic vector hydrophone microstructure is shown in Figure 4, where  $L$  is the length of the beam,  $t$  is the thickness of the beam,  $2a$  is the side length of the center block,  $h$  is the height of the rigid cylinder, and  $r$  is the height of the rigid cylinder.

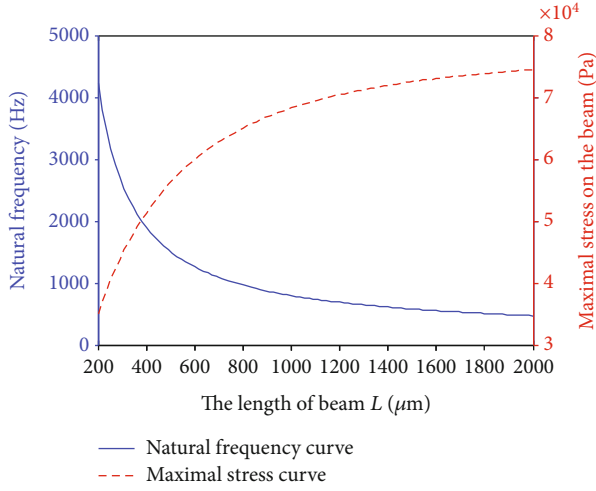


FIGURE 8: Dependence of maximum stress and natural frequency on  $L$ .

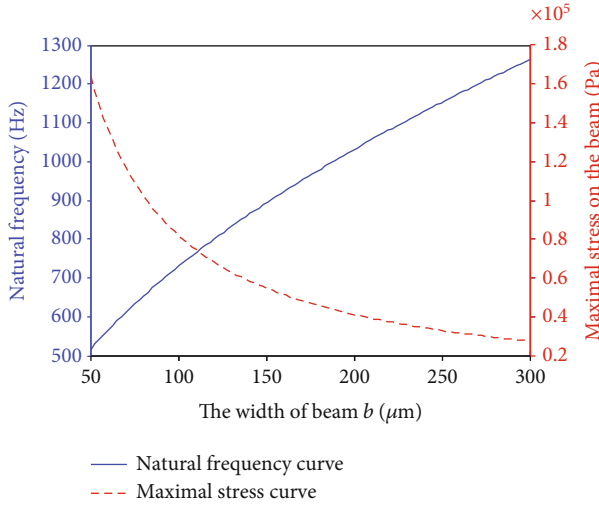


FIGURE 9: Dependence of maximum stress and natural frequency on  $b$ .

The mathematical model analysis of the hydrophone microstructure is based on the following assumptions: (a) compared with rigid cylinder, the effective mass of the four-beam-center block is very small, which can be ignored in the analysis process; (b) the four-beam and the center block is an elastic structure; (c) the rigid cylinder and the frame of the four-beam-center block are rigid. When the rigid cylinder of the hydrophone microstructure is subjected to uniformly distributed loads  $P_x$  in the  $X$  direction.  $P_x$  will produce two components in the center block of the microstructure, that is, the horizontal force  $F_H$  ( $F_H = 2P_x hr$ ) along the  $X$  direction and the moment  $M$  ( $M = P_x h^2 r$ ) around the  $Y$  direction. Establish the mechanical analysis model of the microstructure (as shown in Figures 5–7). Figure 5 shows deformation when subjected to uniformly distributed loads  $P_x$ . Figure 6 shows the force analysis of the center block, and Figure 7 shows the stress of a single cantilever beam.

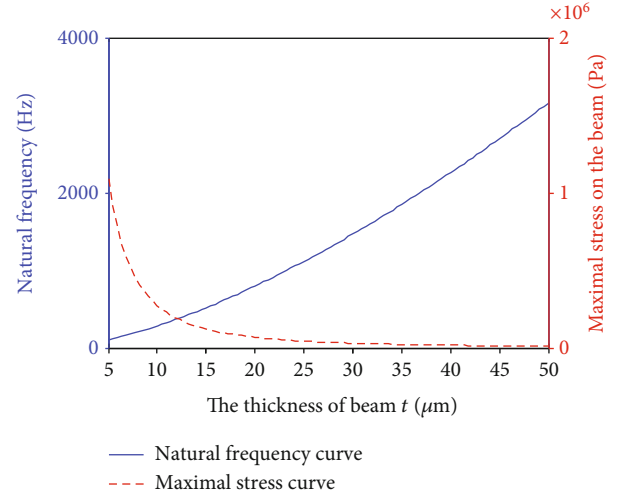


FIGURE 10: Dependence of maximum stress and natural frequency on  $t$ .

Based on the principles of material mechanics and elastic mechanics [23], for any point  $x$  on the cantilever beam, there are:

$$\sum M = 0 \Rightarrow M_{(x)} = -M_1 + F_V(L - x). \quad (5)$$

The vertical upward force  $F_V$  at point  $D$  can be expressed as:

$$F_V = \frac{3(L + 2a)}{L(2L + 3a)} M_1. \quad (6)$$

In Figure 7, the center point of the center block is selected as the research object. Formula (7) can be written as:

$$\sum M = 0 \Rightarrow 2(F_V \cdot a + M_1) = M. \quad (7)$$

By substituting formula (6) into (7), it can be obtained that

$$M_1 = \frac{L(2L + 3a^2)}{4(L^2 + 3aL + 3a^2)} M. \quad (8)$$

Substituting formulas (6) and (8) into (5), moment  $M_{(x)}$  applied at any point on the beam can be expressed as:

$$M_{(x)} = \frac{L^2 + 3aL - 3x(a + L)}{4(L^2 + 3aL + 3a^2)} M. \quad (9)$$

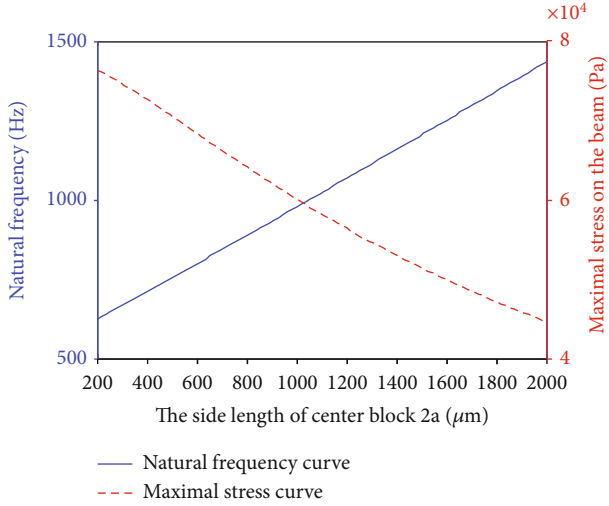


FIGURE 11: Dependence of maximum stress and natural frequency on  $2a$ .

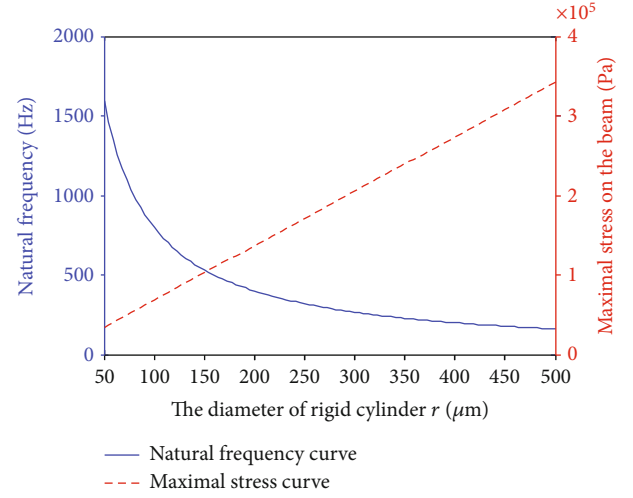


FIGURE 13: Dependence of maximum stress and natural frequency on  $r$ .

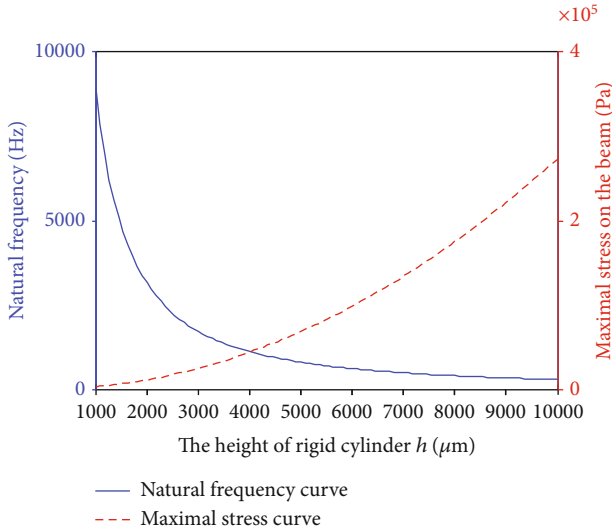


FIGURE 12: Dependence of maximum stress and natural frequency on  $h$ .

Therefore, the stress  $\sigma_{(M(x))}$  of any point  $x$  on the cantilever beam under the action of  $M_{(x)}$  is:

$$\sigma_{(M(x))} = \frac{M_{(x)}}{W} = \frac{L^2 + 3aL - 3x(a+L)}{2/3bt^2(L^2 + 3aL + 3a^2)} M, \quad (10)$$

wherein,  $W$  ( $W = bt^{2/6}$ ) is the bending section modulus of the beam, and  $b$  is the width of the beam.

The stress  $\sigma_{F_H}$  at any point  $x$  of a single cantilever beam under the action of  $F_H$  is:

$$\sigma_{F_H} = \frac{F_H}{bt}. \quad (11)$$

TABLE 1: The geometry parameters of the microstructure.

| Parameters ( $\mu m$ )                   | 1    | 2    |
|--|------|------|
| The length of beam ( $L$ )               | 1000 | 500  |
| The side length of center block ( $2a$ ) | 600  | 600  |
| The width of beam ( $b$ )                | 120  | 80   |
| The thickness of beam ( $t$ )            | 20   | 12   |
| The thickness of center block ( $t$ )    | 20   | 12   |
| The height of rigid cylinder ( $h$ )     | 5000 | 4000 |
| The radius of rigid cylinder ( $r$ )     | 100  | 100  |

TABLE 2: Material property parameters.

| Material       | Density $\rho$ ( $kg/m^3$ ) | Young's modulus ( $10^{11}N/m^2$ ) | Poisson's ratio |
|----------------|-----------------------------|------------------------------------|-----------------|
| Si             | 2330                        | 1.65                               | 0.278           |
| Rigid cylinder | 2320                        | 0.74                               | 0.17            |

Thus, the stress  $\sigma_{(x)}$  at any point  $x$  of a single cantilever beam under the combined action of  $M_{(x)}$  and  $F_H$  is

$$\sigma_{(x)} = \pm \frac{L^2 + 3aL - 3x(a+L)}{(2/3)bt^2(L^2 + 3aL + 3a^2)} M \pm \frac{F_H}{bt}, \quad (12)$$

It can be known from formula (12) that the maximal stress on the beam is on the both ends. That is,  $\sigma_{(0)}$  is maximal (as shown in formula (13)).

$$\sigma(0) = \pm \frac{L^2 + 3aL}{(2/3)bt^2(L^2 + 3aL + 3a^2)} M \pm \frac{F_H}{bt}. \quad (13)$$

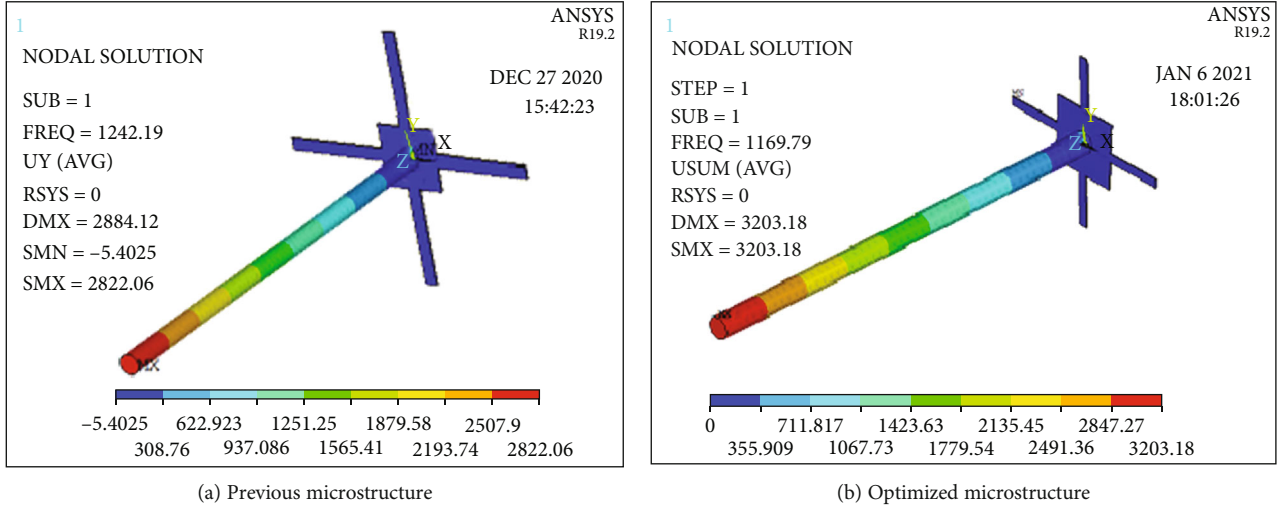


FIGURE 14: The first order modal analysis.

According to material mechanics theory, the stiffness of the microstructure on the  $X$  or  $Y$  direction can be calculated which can be expressed as [23, 24]:

$$K_x = K_y = \frac{2Ebt^3}{Lh^2} \left( \frac{a^2}{L^2} + \frac{a}{L} + \frac{1}{3} \right), \quad (14)$$

where  $E$  is the Young's modulus of silicon material.

The nature frequency of the microstructure is can be expressed as:

$$f = \frac{1}{2\pi} \sqrt{\frac{K}{m}} = \frac{1}{2\pi} \sqrt{\frac{2Ebt^3}{mLh^2} \left( \frac{a^2}{L^2} + \frac{a}{L} + \frac{1}{3} \right)}, \quad (15)$$

where  $m$  is the mass of the rigid cylinder.  $K$  is the stiffness of the microstructure and  $K = K_x = K_y$ .

From formulas (14) and (15), it can be concluded that the natural frequency of the microstructure and the maximum stress on the cantilever beam vary with the microstructural parameters (length, width and height of cantilever, side length of the center block, height and radius of the rigid cylinder) (as shown in Figures 8–13).

From Figures 8–13, it can be seen that the microstructural parameters have different weight effects on the natural frequency of the microstructure and the maximum stress on the beam. And,  $2a$  and  $L$  have almost the same weight effect on the maximum stress and the natural frequency;  $t$  and  $b$  have a greater weight effect on the maximum stress than the natural frequency;  $r$  and  $h$  have a greater weight effect on the natural frequency than the maximum stress. Therefore, MEMS vector hydrophone microstructural parameters can be designed reasonably to obtain the maximum stress, and the natural frequency hardly changes.

**3.2. Optimization Design.** The optimal solution is any feasible solution that makes the objective function obtain the optimal value (maximum or minimum value) in the feasible region.

The maximum stress  $\sigma_{(0)}$  and nature frequency  $f$ , respectively, can be seen as the multivariate functions of the microstructural parameters ( $L, b, t, a, h$ , and  $r$ ) (as shown in formulas (16) and (17)).

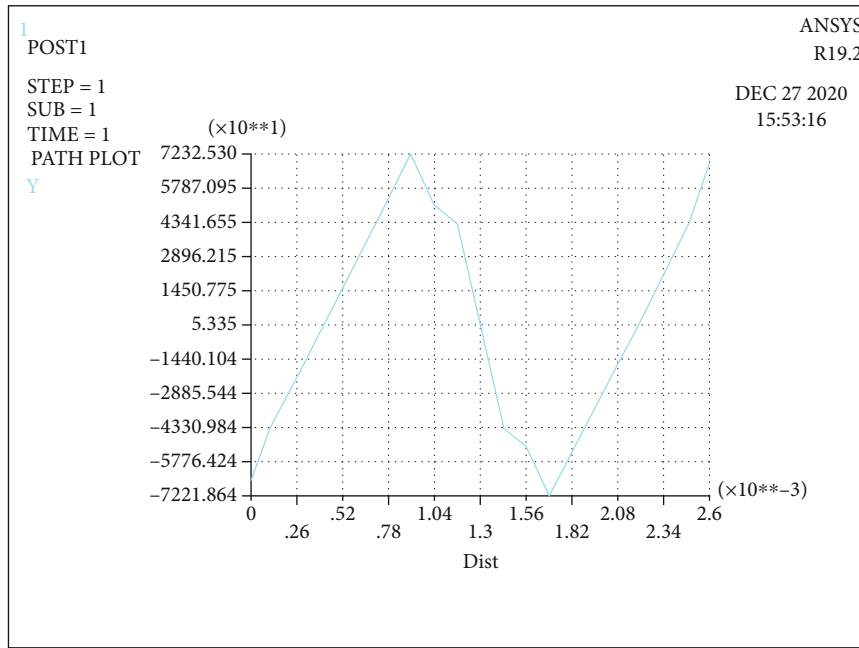
$$\sigma(L, b, t, a, h, r) = \frac{L^2 + 3aL}{(2/3)bt^2(L^2 + 3aL + 3a^2)} M + \frac{F_H}{bt}, \quad (16)$$

$$f(L, b, t, a, h, r) = \frac{1}{2\pi} \sqrt{\frac{2Ebt^3}{mLh^2} \left( \frac{a^2}{L^2} + \frac{a}{L} + \frac{1}{3} \right)}. \quad (17)$$

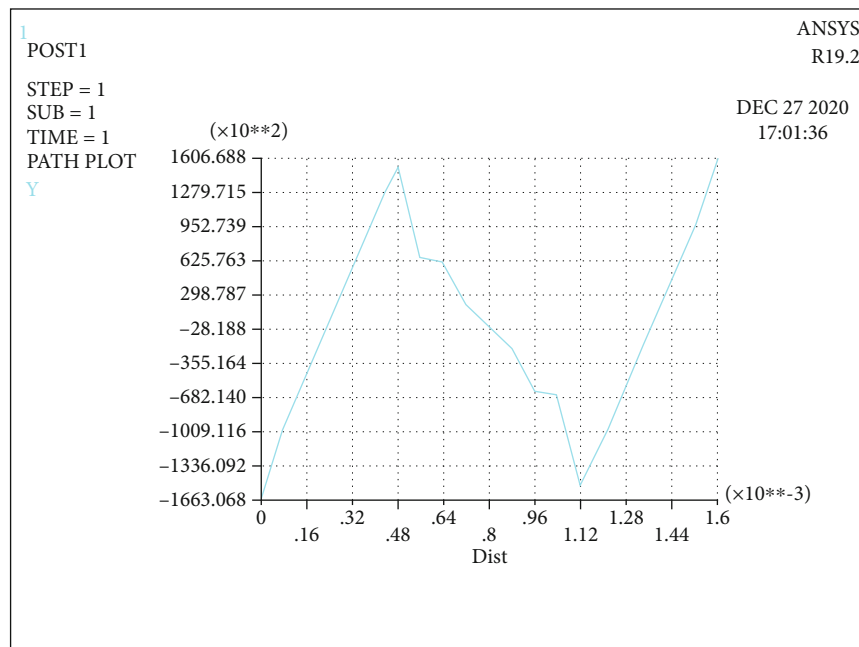
The first set of values ( $L_1, b_1, t_1, a_1, h_1, r_1$ ) as shown in Table 1 is commonly used as the microstructure parameters. According to the actual processing conditions and requirements, the ranges of the variable parameters are set as follows: (1)  $500 \leq L \leq 1500$ , (2)  $80 \leq b \leq 160$ , (3)  $8 \leq t \leq 40$ , (4)  $200 \leq a \leq 300$ , (5)  $2000 \leq h \leq 10000$ , (6)  $100 \leq r \leq 200$ , and (7)  $f(L_1, b_1, t_1, a_1, h_1, r_1) \leq f(L, b, t, a, h, r)$ .  $D(L, b, t, a, h, r)$  is regarded as the feasible zone constituted by the above seven constraint conditions, and  $\sigma(L, b, t, a, h, r)$  is viewed as the objective function. Searching the maximum of  $\sigma(L, b, t, a, h, r)$  in  $D(L, b, t, a, h, r)$  by MATLAB, the optimal solution ( $L_2, b_2, t_2, a_2, h_2, r_2$ ) is obtained when  $\sigma(L, b, t, a, h, r)$  acquire the max (as shown in the second set of values of Table 1).

## 4. Simulation Analysis and Fabrication

**4.1. Simulation Analysis.** The finite element models of the previous microstructure and the optimized microstructure have been, respectively, established by ANSYS software. The material property parameters are shown in Table 2. The modal analysis and static analysis have been carried



(a) Previous microstructure



(b) Optimized microstructure

FIGURE 15: Stress analysis.

out. The nature frequency of the microstructures can be obtained by modal diagrams (as shown in Figure 14). And the stress distribution curves on the beams are shown in Figure 15.

It can be seen from Figures 14 and 15 that the nature frequency of the optimized microstructure is 1170 Hz, which is close to that (1242 Hz) of previous microstructure, and the maximum stress on the beam of the optimized microstructure is 160669 Pa, which is more than twice as much as that (72325 Pa) of previous microstructure.

That is to say, the sensitivity of the optimized microstructure has been doubled, and the nature frequency almost remains unchanged. Thus, the optimization design of the microstructure is feasible.

**4.2. Fabrication.** The four-beam microstructure is fabricated by standard MEMS technology which mainly includes photolithography, oxidation, etching, ion implantation, and sputtering [25, 26]. The main process is shown in Figure 16. (a) An N-type 4-inch SOI (12 μm device layer,



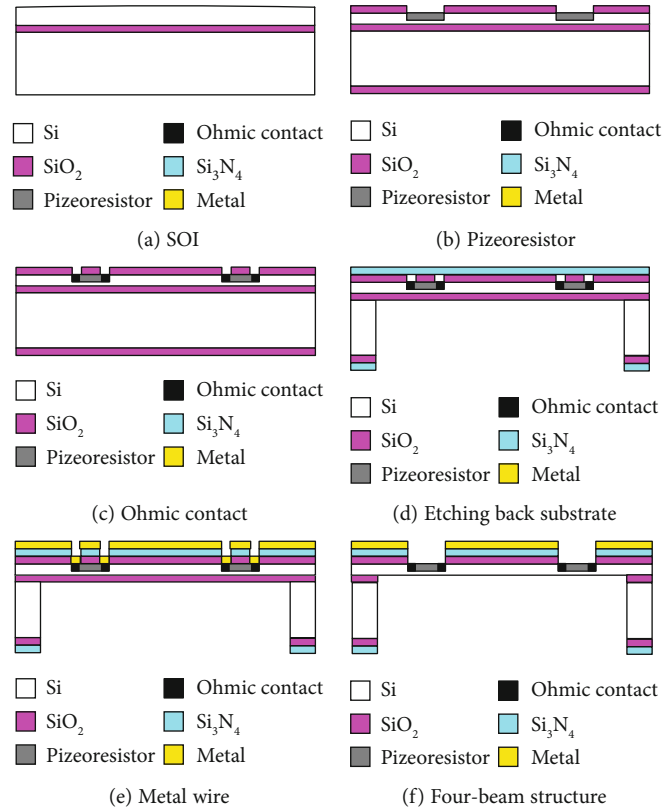


FIGURE 16: The processing technology of the optimized four-beam microstructure.

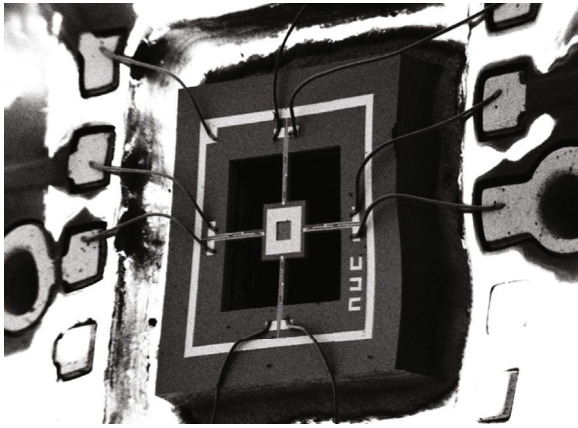


FIGURE 17: SEM diagram of MEMS four-beam microstructure.

$2\ \mu\text{m}$  buried oxide layer, and  $400\ \mu\text{m}$  substrate layer) with crystal plane (100) and crystal orientation  $\langle 100 \rangle$  is prepared. (b) The SOI is oxidized at  $950^\circ\text{C}$  to form  $1000\ \text{\AA}$  SiO<sub>2</sub> on both sides, and the front SiO<sub>2</sub> is etched by ICP to form the piezoresistor windows. The boron ions with 100 keV energy and  $4 \times 10^{18}\ \text{cm}^{-3}$  surface concentration are implanted, and then anneal to form the piezoresistors. (c) The SOI is reoxidized, and the front SiO<sub>2</sub> is etched by ICP to form ohmic contact region. The denser boron ions with 100 keV energy and  $4 \times 10^{21}\ \text{cm}^{-3}$  surface concentration are implanted, and then, the ohmic contacts are formed by annealing. (d)  $1100\ \text{\AA}$  Si<sub>3</sub>N<sub>4</sub> is deposited on both sides of the SOI by PECVD. The

Si<sub>3</sub>N<sub>4</sub> and SiO<sub>2</sub> on the back side of SOI are etched by RIE, and then, etch the backside silicon using KOH and self-stop at the SiO<sub>2</sub> layer. (e)  $500\ \text{\AA}$  Cr and  $1000\ \text{\AA}$  Au are deposited on the front side and etched by iodine water to realize the connection of the Wheatstone bridge. (f) Si<sub>3</sub>N<sub>4</sub> and SiO<sub>2</sub> on the front side are etched by RIE, and SiO<sub>2</sub> on the back side is etched by RIE, and then, the cantilever structure is released.

The four-beam microstructure (MEMS chip) is fabricated as shown in Figure 17. The high aspect ratio microstructure cannot be processed through the current domestic MEMS processing lines, so it is necessary to bond the four-beam microstructure and the rigid cylinder. Then, the two hydrophones (previous one and optimized one) have been fabricated (as shown in Figure 18).

## 5. Performance Test

The calibration tests for these two hydrophones without package have been, respectively, performed in the standing wave barrel with the method of comparison [27]. During testing, one of these two hydrophones (tested hydrophone) and a standard hydrophone are placed in the standing wave barrel filled with silicone oil. The standard hydrophone is the RS-100 piezoelectric sound pressure hydrophone with sensitivity of  $-180\ \text{dB}$  ( $0\ \text{dB ref } 1\ \text{V}/\mu\text{Pa}$ ) and bandwidth of  $20\ \text{Hz} \sim 100\ \text{kHz}$  used as a reference hydrophone for the calibration test. The sensitivity of the tested hydrophone at different frequency can be acquired by comparing the output voltage values of the two hydrophones (tested hydrophone

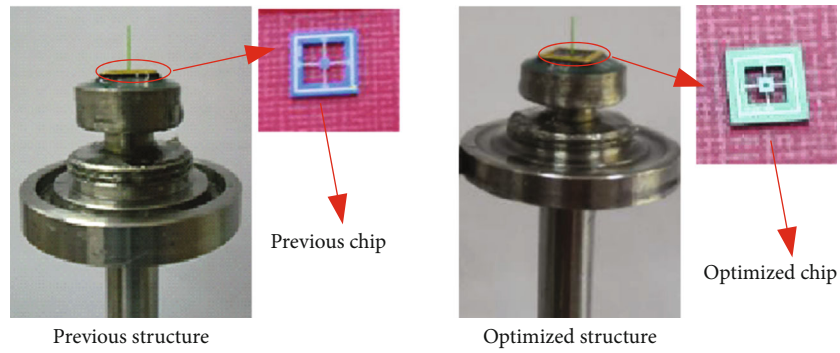


FIGURE 18: The diagram of two hydrophones without package.

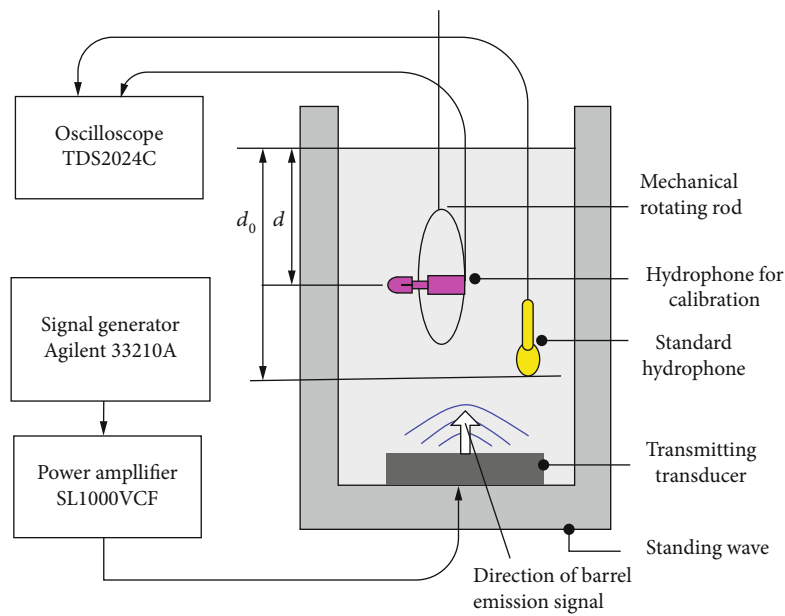


FIGURE 19: Schematic diagram of the calibration device.

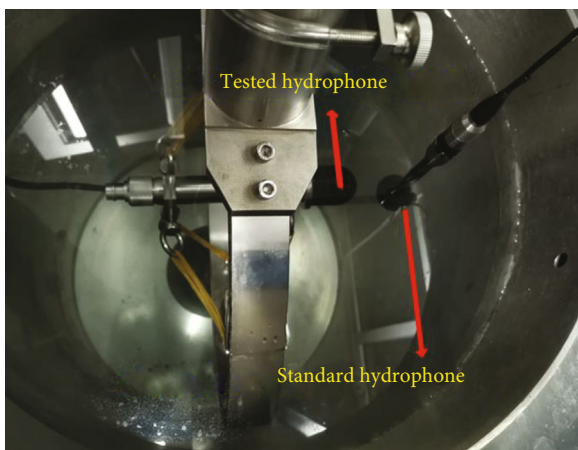


FIGURE 20: The calibration system.

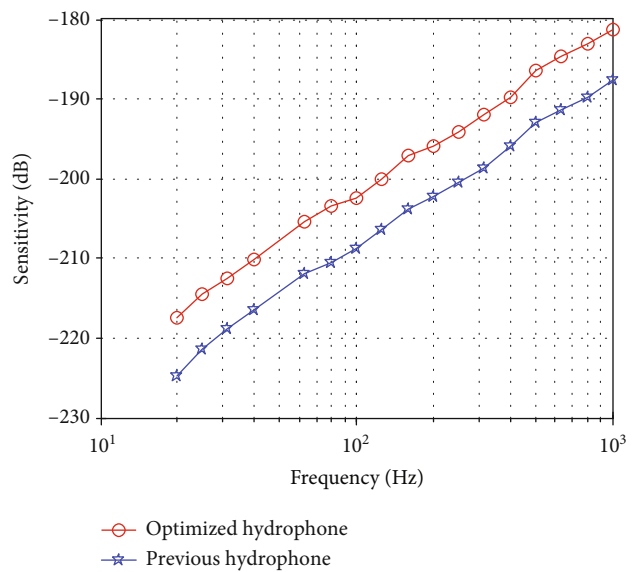


FIGURE 21: The sensitivity curves in X direction.

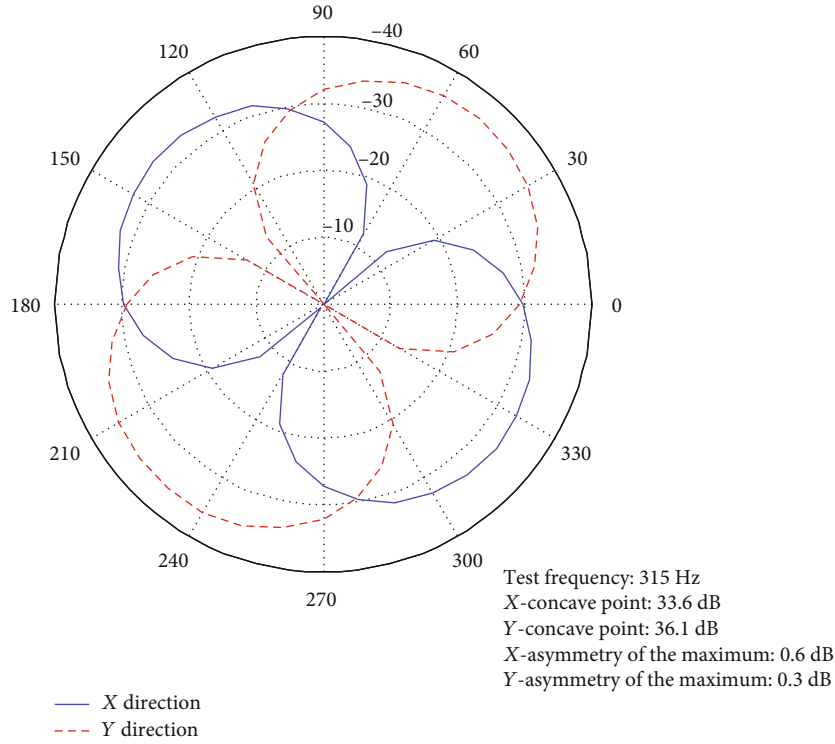


FIGURE 22: Directivity pattern at a frequency of 315 Hz.

and standard hydrophone). The schematic diagram of the calibration devices is shown in Figure 19, and the calibration system is shown in Figure 20. During the testing, data are recorded in one-third-octave frequency points from 20 Hz to 1 kHz. When the sensitivity of X or Y direction is calibrated, it must be made sure that the acoustic wave propagation direction of the standing wave barrel is paralleled to the corresponding maximum sensitivity direction.

The X direction is as an example in this paper. The sensitivity  $M_x$  of the tested hydrophone can be expressed as [27]:

$$M_x = M_0 \frac{e_x}{e_0} \cdot \frac{\sin kd_0}{\cos kd}, \quad (18)$$

where  $M_0$  is the voltage sensitivity of the standard hydrophone;  $e_x$  and  $e_0$  are the open output voltage of the tested hydrophone and the standard hydrophone, respectively;  $d$  is the depth of the tested hydrophone;  $d_0$  is the depth of the standard hydrophone;  $k$  is wave number. The sensitivity testing results of these two hydrophones are shown in Figure 21.

Then, the directivity pattern of the optimized hydrophone is measured by the same equipment as shown in Figure 20. At the tested frequency, rotate the optimized hydrophone from  $0^\circ$  to  $360^\circ$  and record the hydrophone's outputs ( $e_\theta$ ) at each degree. The recorded data should be normalized by formula (19).

$$L = 20 \log \left( \frac{e_\theta}{e_{\max}} \right), \quad (19)$$

where  $e_{\max}$  is the maximum of the outputs. The directivity pattern is obtained by plotting the normalized data ( $L$ ) in polar coordinates. The directivity pattern at 315 Hz is depicted in Figure 22.

From Figure 21, it can be obtained that the sensitivity of the optimized hydrophone is  $-181.2$  dB @1 kHz (0 dB reference  $1 \text{ V}/\mu\text{Pa}$ ), which is about 6.5 dB higher than that of the previous hydrophone, and they all range in working bandwidth from 20 Hz to 1000 Hz. Figure 22 shows that the optimized hydrophone has a good directional pattern in the form of an "8" shape and excellent symmetry property. Therefore, the optimized microstructure can improve the sensitivity of the hydrophone and maintain the same working bandwidth with the previous microstructure.

## 6. Conclusion

To better realize the engineering application of the MEMS vector hydrophone, this paper introduces the optimal designs of the hydrophone microstructure to further improve its sensitivity without changing working bandwidth. The mechanics analysis of the microstructure is carried out, and the objective function and feasible region are established to calculate the optimal solution of the microstructure. And the optimal designs have been proved through ANSYS simulation.

Then, the optimized microstructure has been fabricated by the standard MEMS technology. Finally, the two hydrophones (previous one and optimized one) have been fabricated and tested in standing wave barrel to verify the feasibility of the optimization. The test results show that the

receiving sensitivity of the optimized hydrophone reaches up to  $-181.2$  dB@1 kHz (0 dB reference  $1$  V/ $\mu$ Pa), improved 6.5 dB, and whose working bandwidth is 20–1000 Hz without changed. Moreover, the optimized hydrophone has superior “8” shape directivity and concave point depth. Thus, the performance of the optimized hydrophone has been greatly improved compared with that of the previous hydrophone. The optimization provides new ideas to improve the performance of MEMS bionic vector hydrophone and lays the further foundation for its engineering application.

## Data Availability

The data used to support the findings of this study are available from the corresponding author upon request.

## Conflicts of Interest

The authors declare that there is no conflict of interest regarding the publication of this paper.

## Acknowledgments

This work was funded by the National Natural Science Foundation of China (Grant nos. 51805154 and 51975191) and Scientific Research Foundation of Hubei University of Technology (GCRC2020010).

## References

- [1] S. L. Fan, *Thinking of China's Sea Power and Ocean Strategy*, [Ph.D. thesis], Central Party School, 2007.
- [2] D. H. Liu, C. C. Lian, F. M. Liu, C. J. Wang, R. X. Ji, and X. X. Li, “Some views on ocean strategic layout of the Atlantic Ocean for China,” *Ocean Development and Management*, vol. 33, no. 5, pp. 3–7, 2016.
- [3] S. T. Yang, *The Research of Deep-Water Vector Hydrophone*, [Ph.D. thesis], Harbin Institute of Technology, 2010.
- [4] K. Kim, *Investigation of an Underwater Acoustic Vector Sensor*, [Ph.D. thesis], The Pennsylvania State University, 2002.
- [5] G. P. Zhang, C. Zheng, and W. S. Lin, “Steering acoustic intensity estimator using a single acoustic vector hydrophone,” *Journal of Sensors*, vol. 2018, Article ID 8526092, 10 pages, 2018.
- [6] M. Liu, L. Nie, G. Zhang, W. Zhang, and J. Zou, “Realization of a composite MEMS hydrophone without left-right ambiguity,” *Sensors and Actuators A: Physical*, vol. 272, pp. 231–241, 2018.
- [7] P. Amiri, Z. Kordrostami, and K. Hassanli, “Design of a MEMS bionic vector hydrophone with piezo-gated MOSFET read-out,” *Microelectronics Journal*, vol. 98, article 104748, p. 7, 2020.
- [8] A. Hossain and A. Mian, “Four-terminal square piezoresistive sensors for MEMS pressure sensing,” *Journal of Sensors*, vol. 2017, Article ID 6954875, 11 pages, 2017.
- [9] J. Kim, S. Pyo, and Y. Roh, “Analysis of a thickness-shear mode vibrator for the accelerometer in vector hydrophones,” *Sensors and Actuators, A: Physical*, vol. 266, pp. 9–14, 2017.
- [10] B. A. Ganji, M. S. Nateri, and M. Dardel, “Design and modeling of a novel high sensitive MEMS piezoelectric vector hydrophone,” *Microsystem Technologies*, vol. 24, no. 4, pp. 2085–2095, 2018.
- [11] C. Xue, S. Chen, W. Zhang, B. Zhang, G. Zhang, and H. Qiao, “Design, fabrication, and preliminary characterization of a novel mems bionic vector hydrophone,” *Microelectronics Journal*, vol. 38, no. 10–11, pp. 1021–1026, 2007.
- [12] C. Xue, Z. Tong, B. Zhang, and W. Zhang, “A novel vector hydrophone based on the piezoresistive effect of resonant tunneling diode,” *IEEE Sensors Journal*, vol. 8, no. 4, pp. 401–402, 2008.
- [13] M. Liu, G. Zhang, X. Song, Y. Liu, and W. Zhang, “Design of the monolithic integrated array MEMS hydrophone,” *IEEE Sensors Journal*, vol. 16, no. 4, pp. 989–995, 2016.
- [14] Q. Xu, G. Zhang, Y. Zhao et al., “New insight into contradictive relationship between sensitivity and working bandwidth of cilium MEMS bionic vector hydrophone,” *Journal of Micromechanics and Microengineering*, vol. 29, no. 11, article 115016, 2019.
- [15] Y. Liu, R. Wang, G. Zhang et al., ““Lollipop-shaped” high-sensitivity microelectromechanical systems vector hydrophone based on parylene encapsulation,” *Journal of Applied Physics*, vol. 118, no. 4, article 044501.1, 2015.
- [16] G. Zhang, J. Ding, W. Xu et al., “Design and optimization of stress centralized MEMS vector hydrophone with high sensitivity at low frequency,” *Mechanical Systems and Signal Processing*, vol. 104, pp. 607–618, 2018.
- [17] W. Xu, Y. Liu, G. Zhang et al., “Development of cup-shaped microelectromechanical systems-based vector hydrophone,” *Journal of Applied Physics*, vol. 120, no. 12, article 124502, 2016.
- [18] Q. Xu, G. Zhang, J. Ding et al., “Design and implementation of two-component cilia cylinder MEMS vector hydrophone,” *Sensors and Actuators, A: Physical*, vol. 277, pp. 142–149, 2018.
- [19] L. Zhang, Q. Xu, G. Zhang et al., “Design and fabrication of a multipurpose cilia cluster MEMS vector hydrophone,” *Sensors and Actuators, A: Physical*, vol. 296, pp. 331–339, 2019.
- [20] S. Ji, L. Zhang, W. Zhang et al., “Design and realization of dumbbell-shaped ciliary MEMS vector hydrophone,” *Sensors and Actuators, A: Physical*, vol. 311, p. 9, 2020.
- [21] X. Yang, Q. Xu, G. Zhang et al., “Design and implementation of hollow cilium cylinder MEMS vector hydrophone,” *Measurement*, vol. 168, article 108309, 2021.
- [22] K. V. Meena, R. Mathew, J. Leelavathi, and A. R. Sankar, “Performance comparison of a single element piezoresistor with a half-active Wheatstone bridge for miniaturized pressure sensors,” *Measurement*, vol. 111, pp. 340–350, 2017.
- [23] S. Chen, *Research of MEMS Bionic Vector Hydrophone Based on Silicon*, [Ph.D. thesis], The North University of China, 2008.
- [24] Z. M. Jian, G. J. Zhang, M. R. Liu, and W. D. Zhang, “Micro-structure optimization design of the MEMS bionic vector hydrophone,” *Micronanoelectronic Technology*, vol. 51, no. 9, pp. 576–582, 2014.
- [25] H. Guo, X. Li, Q. Zhu et al., “Imaging nano-defects of metal waveguides using the microwave cavity interference enhancement method,” *Nanotechnology*, vol. 31, no. 45, article 455203, 2020.
- [26] M. Liu, L. Nie, S. Li et al., “Array MEMS vector hydrophone oriented at different direction angles,” *Sensors*, vol. 19, no. 19, article 4282, 2019.
- [27] J. X. Fan, *The Study of Vector Hydrophone Calibration Equipment*, [M.S. thesis], Harbin Engineering University, 2007.